Pressure transient analysis to investigate a coupled fracture corridor and a fault damage zone causing an early thermal breakthrough in the North Alpine Foreland Basin

Fadel, Mohamed; Meneses Rioseco, Ernesto; Bruna, Pierre Olivier; Moeck, Inga

DOI
10.1016/j.geoen.2023.212072

Publication date
2023

Document Version
Final published version

Published in
Geoenergy Science and Engineering

Citation (APA)
Fadel, M., Meneses Rioseco, E., Bruna, P. O., & Moeck, I. (2023). Pressure transient analysis to investigate a coupled fracture corridor and a fault damage zone causing an early thermal breakthrough in the North Alpine Foreland Basin. *Geoenergy Science and Engineering*, *229*, Article 212072. https://doi.org/10.1016/j.geoen.2023.212072

229 (2023) 212072

Contents lists available at ScienceDirect

Geoenergy Science and Engineering

journal homepage: www.sciencedirect.com/journal/geoenergy-science-and-engineering

Pressure transient analysis to investigate a coupled fracture corridor and a fault damage zone causing an early thermal breakthrough in the North Alpine Foreland Basin

Mohamed Fadel [a,b,d,*], Ernesto Meneses Rioseco [a,b], Pierre-Olivier Bruna [c], Inga Moeck [a,b]

[a] Leibniz Institute for Applied Geophysics (LIAG), Stilleweg 2, 30655, Hannover, Germany
[b] Georg-August-Universität Göttingen, Goldschmidtstr. 3, 37077, Göttingen, Germany
[c] Delft University of Technology, Stevinweg 1, 2628 CN, Delft, the Netherlands
[d] Vulcan Energy Subsurface Solutions GmbH, An der Raumfabrik 33 c, 76227, Karlsruhe, Germany

ARTICLE INFO

Keywords:
Pressure transient analysis
Premature thermal breakthrough
Double porosity models and discreet fracture network
Fracture corridors
Upper Jurassic carbonates
North Alpine foreland Basin

ABSTRACT

The heterogeneity of the Upper Jurassic carbonate reservoir (Malm reservoir) beneath the North Alpine Foreland Basin has a significant influence on the mass and heat flow processes during geothermal exploitation. Geophysical borehole data revealed that sub-seismic scale fractures and karstified fractures occur at the inflow zones of deep geothermal wells. However, pressure transient analysis (PTA) in some previous studies concluded that it is difficult to detect the influence of sub-seismic scale features, suggesting that radial flow regime is dominant. Accordingly, a regional thermal-hydraulic model adopted the equivalent porous medium (EPM) approach, homogenizing the sub-seismic scale reservoir heterogeneities; however, unable to detect an early thermal breakthrough (ETB) in a geothermal doublet located SE of Munich. We apply PTA on three buildup tests belonging to that doublet following a deterministic approach to constrain the reservoir type by interpreting the pressure derivative (PD) plots constrained by geophysical and geological data. We derive the magnitudes of the reservoir hydraulic parameters by matching the PD plots with the selected interpretation models. We find that clustered fractures have a significant influence on the reservoir hydraulics, evidenced by trough-shaped curves in the PD plots. Linear flow regime interpreted from the interference test between the two wells indicates permeability anisotropy, which may have caused the ETB. Geophysical data interpretations indicate that these fractures correspond to a coupled fault damage zone and a fracture corridor. Finally, we present a fit-for-purpose 2D discrete fracture network model utilizing the PTA results to match our analytically calibrated model. Our study offers a potential hydraulic explanation to the cause of the ETB highlighting the importance of integrating multi-scale/disciplinary data sets to improve the reliability of dynamic reservoir models, based on which, economic-related decisions are made.

1. Introduction

The transformation of the energy sector in Germany requires optimized utilization concepts of renewable resources for a sustainable transition (Schiffer and Trüby, 2018). Especially after the recent political escalations, geothermal energy is a strong alternative for the gas imports to the German heat production market (Fischedick, 2022).

Many studies investigated the German geothermal resources potential hosted in sedimentary settings, such as the North Alpine Foreland Basin (NAFB), the Upper Rhine Graben, and the North German Basin (Agemar et al., 2014; Dornstadter et al., 1999; Franz et al., 2018; Lüschen et al., 2014; Moeck, 2014). Evaluating, modeling, and optimally managing the geothermal energy extraction processes from sedimentary settings require characterizing the reservoir heterogeneity, which is key for dynamic reservoir models to properly predict the reservoir performance, e.g., defining thermal breakthrough time (Bundschuh and Arriaga, 2011).

One of the main methods used to characterize the dynamic behavior of petroleum and geothermal reservoirs is pressure transient analysis (PTA) of well testing data (Bourdet, 2002; Da Prat, 1990; Streltsova, 1988; Zarrouk and McLean, 2019). This method analyses the observed changes in the reservoir pressure due to induced changes to the flow rate by production or injection. The interpretation of such data focuses on

* Corresponding author. Leibniz Institute for Applied Geophysics (LIAG), Stilleweg 2, 30655, Hannover, Germany.
E-mail address: mohamed.fadel@leibniz-liag.de (M. Fadel).

https://doi.org/10.1016/j.geoen.2023.212072
Received 10 October 2022; Received in revised form 8 June 2023; Accepted 20 June 2023
Available online 1 July 2023

Abbreviations

BU2	buildup test for the injection well
BU3	buildup test for the interference test
BU1	buildup test for the production well
EPM	equivalent porous medium
GMA	Greater Munich Area
IWell	injection well
MD	measured depth
mD	milliDarcy
NAFB	North Alpine Foreland Basin
k	permeability
PD	pressure derivative
PTA	pressure transient analysis
PWell	production well
MD	slope
TVD	true vertical depth
TVT	true vertical thickness
UHG	Unterhaching
Malm reservoir	Upper Jurassic carbonates

the transient pressure period of a well test before steady state or pseudo steady state flow is reached. The analysis of the transient pressure change can characterize the wellbore condition and the reservoir system type including its hydraulic parameters (e.g., permeability, storativity) and the reservoir boundaries type (e.g., closed, infinite-acting, channel, or sealed). Bourdet et al. (1983) introduced the pressure derivative (PD) method, which eased the evaluation of well testing data, and it is now a standard method in the industry. The characteristic response of flow regimes is easier to detect utilizing the PD, which constitutes a major advantage compared with simple pressure curve analysis (Clark and Van Golf-Racht, 1985).

Despite the efforts made the reliability of PTA decreases with increasing the reservoir heterogeneity/complexity. The non-unique response of different reservoir model systems is one of the problems faced by reservoir engineers. Kuchuk et al. (2015) showed field examples of naturally fracture reservoirs, where the PD plots displayed different responses, even though the reservoir type is similar. Accordingly, the integration of multi-disciplinary data sets (static: applied geophysics, and dynamic: PTA) is extremely important to accurately characterize the reservoir and define its type (Bourdet, 2002; Egya et al., 2022; Kuchuk et al., 2015; Nosjean et al., 2020; Streltsova, 1988).

The Upper Jurassic carbonates (Malm reservoir) beneath the NAFB in the Greater Munich Area (GMA) is one of the main low-enthalpy hydrothermal reservoirs in Middle Europe (Agemar et al., 2014; Fadel et al., 2022; Moeck, 2014). The Malm reservoir consists of heterogeneous carbonate rocks, comprising lateral/vertical lithofacies changes, fault zones, diffuse and clustered fractures, karstification, and diagenetic processes (Fadel et al., 2022; Homuth et al., 2015; Wolfgramm et al., 2007). It accommodates favorable conditions for geothermal use, such as high flow rates reaching 150 liter/sec and temperatures ranging between 80 °C and 150 °C.

The increase in geothermal energy production from the Malm reservoir in Munich propelled the application of reservoir management approaches to ensure geothermal energy extraction sustainability by mitigating the occurrence of early thermal breakthrough (ETB) and minimizing thermal-hydraulic encroachments into adjacent projects (Blank et al., 2021; Dussel et al., 2016; Meneses Rioseco et al., 2018). Analysis of well testing data has been continuously utilized to characterize the dynamic behavior of the Malm reservoir and to locally calibrate thermal-hydraulic numerical models.

According to Konrad et al. (2019), Savvatis (2012) evaluated pumping tests of 41 deep geothermal wells penetrating the Malm reservoir. The author stated that 37 wells exhibited a radial flow regime, where the hydraulic relevance of sub-seismic features cannot be definitively assessed. However, Savvatis (2012) also observed clear indications from some of the borehole data that the inflow zones are characterized by fractures, faults, and/or karstification.

Ortiz Rojas et al. (2018) identified bilinear flow regime in the Malm reservoir section at the Unterhaching (UHG) Gt2 deep geothermal well. The authors interpreted a bilinear flow combined with constant pressure boundary from the PD plots. The bilinear flow indicates that the brine initially flows from the fractures of the damage zone into the wellbore, followed by flow from the surrounding matrix to the fractures. The constant pressure boundary was interpreted as an infinite conductive fault, indicating that the UHG Main fault acts as a conduit.

Konrad et al. (2019) worked on identifying the parameter range of the hydraulic properties between fault zones and the matrix of the Malm reservoir, which controls the occurrence of different flow regimes. The matrix was defined as a continuum domain of equivalent hydraulic properties, homogenizing the sub-seismic scale heterogeneities (e.g., karstification, fractures, and lithofacies change). The fault damage zone is modelled as a block of continuum property, where its thickness is set as a variable in their parameter sweep range. Konrad et al. (2021) applied 90 million parameter combinations numerically, suggesting that it is possible for fault damage zones to be transparent in well testing data, where targeting those faults can significantly increase the wells productivity. Direct geophysical and geological data to quantitatively characterize the fault zone was not presented in the authors study (e.g., thickness).

Schulz et al. (2012) provided for the first time a regional scale static model of the Malm reservoir covering the whole GMA. Dussel et al. (2016) applied dynamic reservoir simulation to that model to investigate the hydraulic and thermal interference of 28 geothermal wells in the Malm reservoir. The regional scale compelled the authors to divide the Malm into a layered composite homogeneous reservoir, utilizing the equivalent porous medium (EPM) approach. The authors concluded that the advancement of the cold-water front (after 50 years of simulation) is limited to the close vicinity of the injection wells, where the hydraulic influence between the projects is less than 1 bar.

Contrary to the predictions of Dussel's et al. (2016) model, an ETB occurred in one of the investigated doublets after only three years of operation (Fadel et al., 2022). This represents the first thermal breakthrough case within a sedimentary geothermal reservoir in Germany.

Wadas and von Hartmann (2022) applied seismic inversion, building a porosity model of the Malm reservoir based on utilizing an acoustic impedance model of a 3D seismic data and porosity logs of the Schäftlarnstraße geothermal site, which is located 10 km NW of Fadel et al. (2022)'s study. The authors concluded that features like karst, fractures, faults, and diagenetic processes form a dual porosity system. The authors recommended including those features in the permeability model, because a direct correlation between matrix porosity and reservoir permeability is not viable. Moreover, integrating flow meter and image logs concluded that karstification and intense fracturing are coinciding with the inflow zones of the wells (Bauer et al., 2021).

Fadel et al. (2022) provided a conceptual local scale hydrogeological model for the reservoir of the geothermal doublet that experienced the ETB. The authors applied seismic and sub-seismic scale analysis to interpret the static reservoir characteristics. By correlating location of the inflow zones with the coinciding sub-seismic scale fractures and the seismic scale structures, the authors interpreted the existence of a fracture corridor striking NW coupled with a fault damage zone. This system induces anisotropic permeability, which possibly caused the ETB. Finally, the authors recommended considering fractured reservoir models of double porosity to simulate the mass and heat flow in the study area.

As presented, the EPM approach has been commonly employed in dynamic reservoir models to represent the Malm reservoir rock. However, the heterogeneity of the permeability structure of the Malm

reservoir rock contradicts the published results of the PTA by some authors, suggesting that radial flow is dominant. In particular, for the southern part of the GMA, where the impact of karstification reduces, the use of the EPM approach may not be suitable (Birner, 2013; Zosseder et al., 2022). This is because other sub-seismic scale features may have a more significant impact on the mass and heat flow within the reservoir (Bauer et al., 2021; Bohnsack et al., 2020; Dussel et al., 2016; Fadel et al., 2022; Homuth, 2014; Homuth et al., 2015; Koch, 2000; Mraz et al., 2018; Wadas and von Hartmann, 2022).

In this paper, we integrate for the first time direct geological and geophysical observations with well testing data in the GMA to characterize the dynamic behavior of the reservoir. Moreover, this study answers a key question if the influence of the sub-seismic scale heterogeneities (e.g., sub-seismic scale fractures/karst in the matrix) can be detected from well testing data. In our approach, we utilize PTA to the buildup tests of the geothermal doublet where the ETB occurred. Our main objectives are to interpret the reservoir system type, the dominating reservoir boundaries, and to derive the magnitudes for the reservoir hydraulic properties. We apply the PD method according to Bourdet (2002) to interpret the buildup phases of the active wells and of an interference test. We reduce uncertainty raised by the non-uniqueness nature of the problem setting by integrating direct observations from geophysical data taking into account the findings of Fadel et al. (2022), Wadas and von Hartmann (2022), and Bauer et al. (2021). Afterwards, we match analytically the PD plots for validating the selected interpretation models. Finally, the derived magnitudes of the hydraulic variables are utilized in parameterizing a fit-for-purpose 2D numerical model to calibrate it with the matched analytical model. This study provides a potential hydraulic explanation to the ETB at local scale, following a deterministic approach by integrating the static reservoir nature with the dynamic observations.

2. Overview on the project data and the reservoir setting

2.1. Doublet setting

The geothermal doublet where the ETB occurred is located 16 km southeast of Munich and is composed of an injection and a production well labeled as IWell and PWell, respectively (Figs. 1 and 2a). The total geothermal capacity of the doublet is 10 MW, feeding a district heating network and an Organic Rankin Cycle power plant for electricity generation (Fadel et al., 2022). The doublet is drilled from the same drilling site deviating at high angle to their targets. The PWell is completed with an 800 m (measured depth, MD) openhole section, whereas, the IWell is completed with a perforated liner of approximately 900 m MD (Fig. 1). The lateral distance between the two wells at the reservoir top (Top Purbeckian) is between 1030 and 1050 m. As shown in Fig. 1, the reservoir vertical section comprises the Purbeckian and the Upper Jurassic named as the Malm reservoir.

2.2. Geology and tectonic setting of the Malm reservoir

The Malm reservoir in the area of interest consists of 450 m naturally fractured and karstified carbonates. The deposition of the Malm carbonates occurred in a shallow passive shelf environment, where lagoonal and reefal buildups carbonate facies were identified

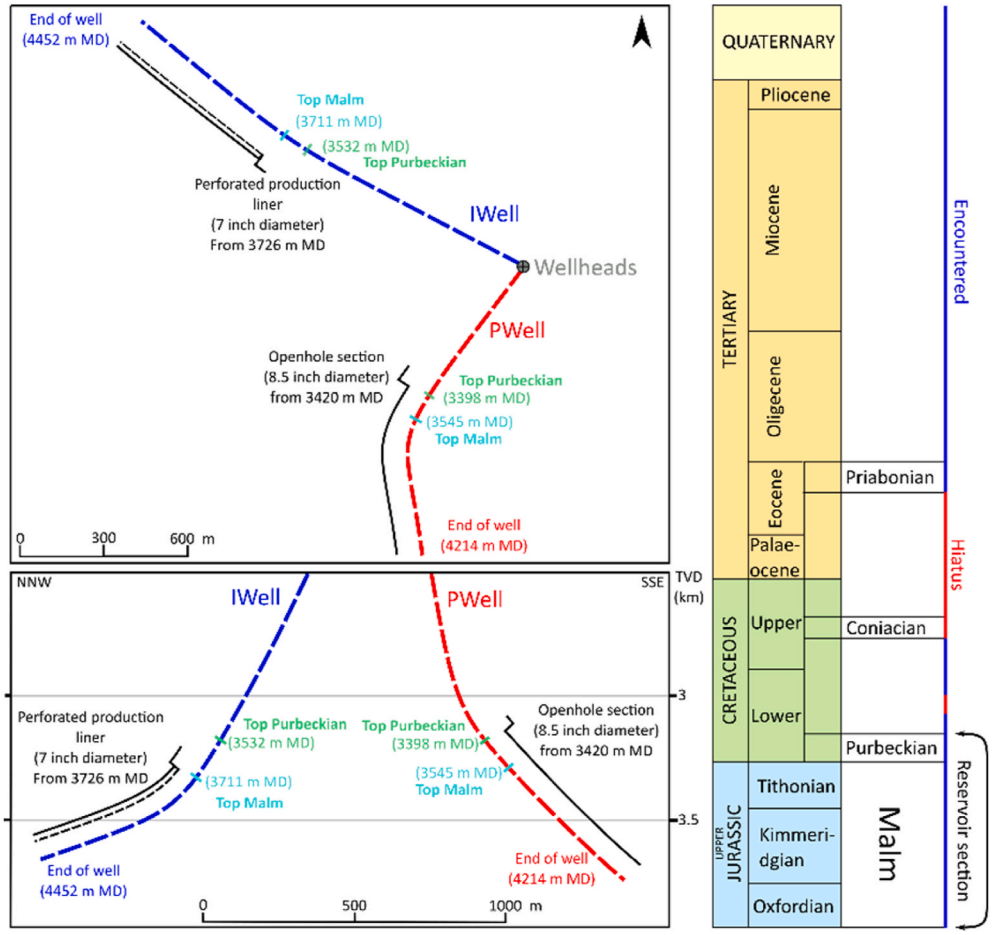

Fig. 1. Map (top) and vertical cross-section (bottom) views of the IWell and the PWell well paths, completion, and markers depth. Right side displays the encountered stratigraphic sequences in both wells (after Fadel et al., 2022).

(Leinfelder, 2001; Meyer and Schmidt-Kaler, 1990). According to the Malm paleo-depositional environment, reefal buildup mounds of anticline shape (paleo-highs) constitute the massive facies type in the reservoir. Whereas, lagoonal beddings of flat topography (paleo-lows) constitute the bedded facies (Meyer and Schmidt-Kaler, 1990; Pawellek and Aigner, 2004; Schmid et al., 2005). The lateral change in the reservoir lithofacies between massive and bedded facies can be distinguished from seismic data in the Malm reservoir (Fadel et al., 2021; Lüschen et al., 2014; Thomas et al., 2010; von Hartmann et al., 2012). As displayed in Fig. 2b, the PWell penetrate a paleo-high of chaotic seismic signature, while the IWell is penetrating a paleo-low structure of relatively stronger seismic amplituds.

The convergence of the African and the European plates is the main tectonic activity with a significant impact on the reservoir structural setting. It occurred during Late Cretaceous (Coniacian - Santonian), which resulted in the closure of the Tethys Ocean and the evolution of the Alpine Orogeny (Bachmann et al., 1987; Freudenberger and Schwerd, 1996). The accumulated nappes of the orogeny applied local burden on the hinge of the European plate, exerting a flexure and a local tension on the Malm platform (Bradley and Kidd, 1991). Normal faults striking W-E to NE-SW penetrating the Malm reservoir are associated with this flexural event. As shown in Fig. 2a and 2b, faults of small throw are found at the vicinity of the wells forming stepping normal faults dipping towards the north or the south. To the far northern and southern direction, normal faults of large throw (i.e. between 200 and 260 m) bound the geothermal reservoir. We label them as the Northern Fault Inventory and the Southern Fault Inventory. Both fault inventories form a 3-4 km graben structure where the investigated doublet sits at its center (Fig. 2b). Reinecker et al. (2010) analyzed the present-day stress field indicators in wellbores (e.g., breakouts and tensile induced fractures) in the NAFB. The authors concluded that the Alpine topography exerts a gravitational force controlling the stress pattern within the NAFB. Strike-slip faulting regime is currently dominating the Malm reservoir where SHmax (S1) is N-S ± 20° (Budach et al., 2017; Fadel et al., 2021; Meneses Rioseco et al., 2022; Reinecker et al., 2010; Ziegler et al., 2016).

2.3. Reservoir static characteristics

In this section, we summarize an update to the main findings recently published by Fadel et al. (2022), who investigated the static characteristics of the reservoir at seismic and sub-seismic scales. This chapter provides insight on the static characteristics of the Malm reservoir in the study area.

2.3.1. Facies distribution

The paleotopography of the Top Malm horizon delineates various elevated and bedded structures representing paleo-highs and paleo-lows (Fig. 3a). The geothermal doublet is bounded from NE and SW by two paleo-highs. The IWell is penetrating a paleo-low, while the PWell is

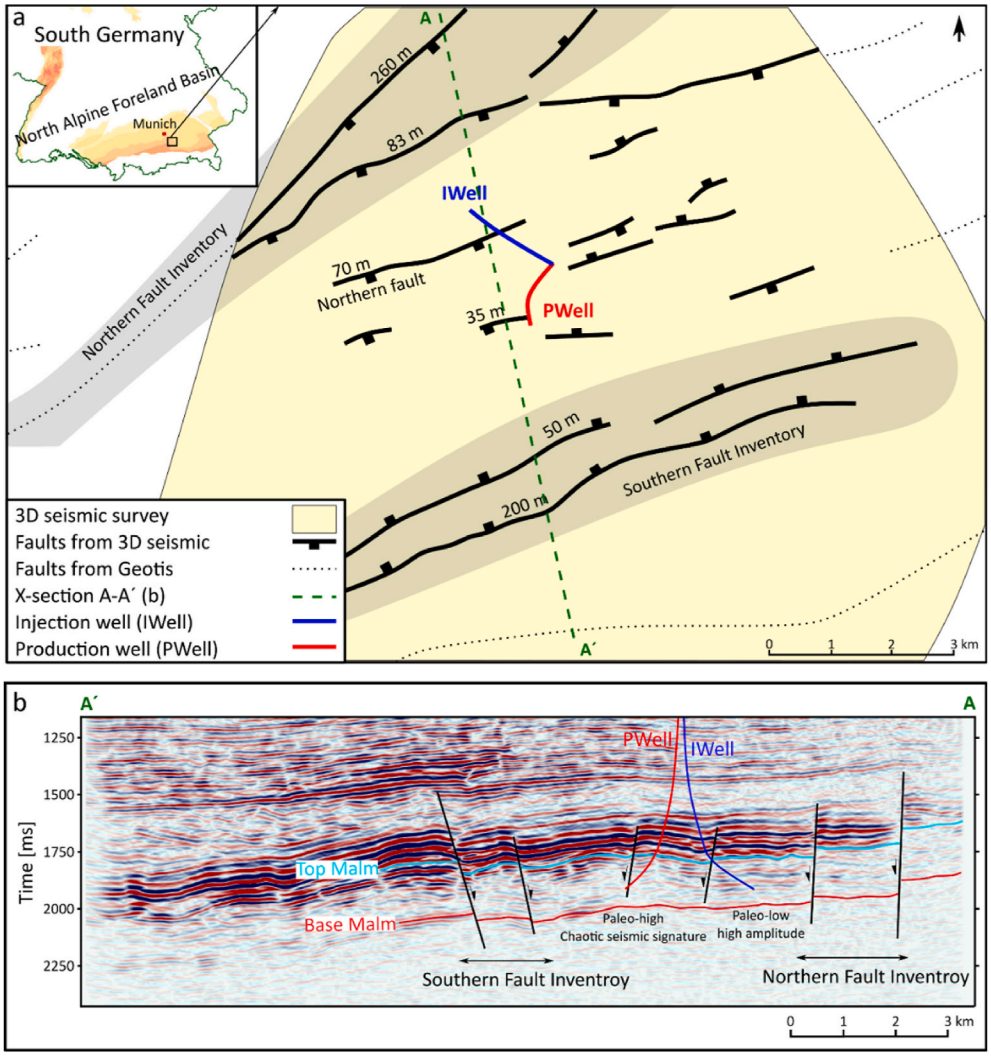

Fig. 2. Structural and facies setting of the investigation area derived from 3D seismic data and GeotIS (2022). a) Location of the geothermal doublet and map view of the faults inventory (numbers beside each fault represent throw magnitudes). b) Time domain seismic cross-section A-A′ delineating the fault structures and the change in the seismic amplitude signature between the vicinities of the PWell and the IWell projections. Top and Base Malm are the top and the base of the geothermal reservoir.

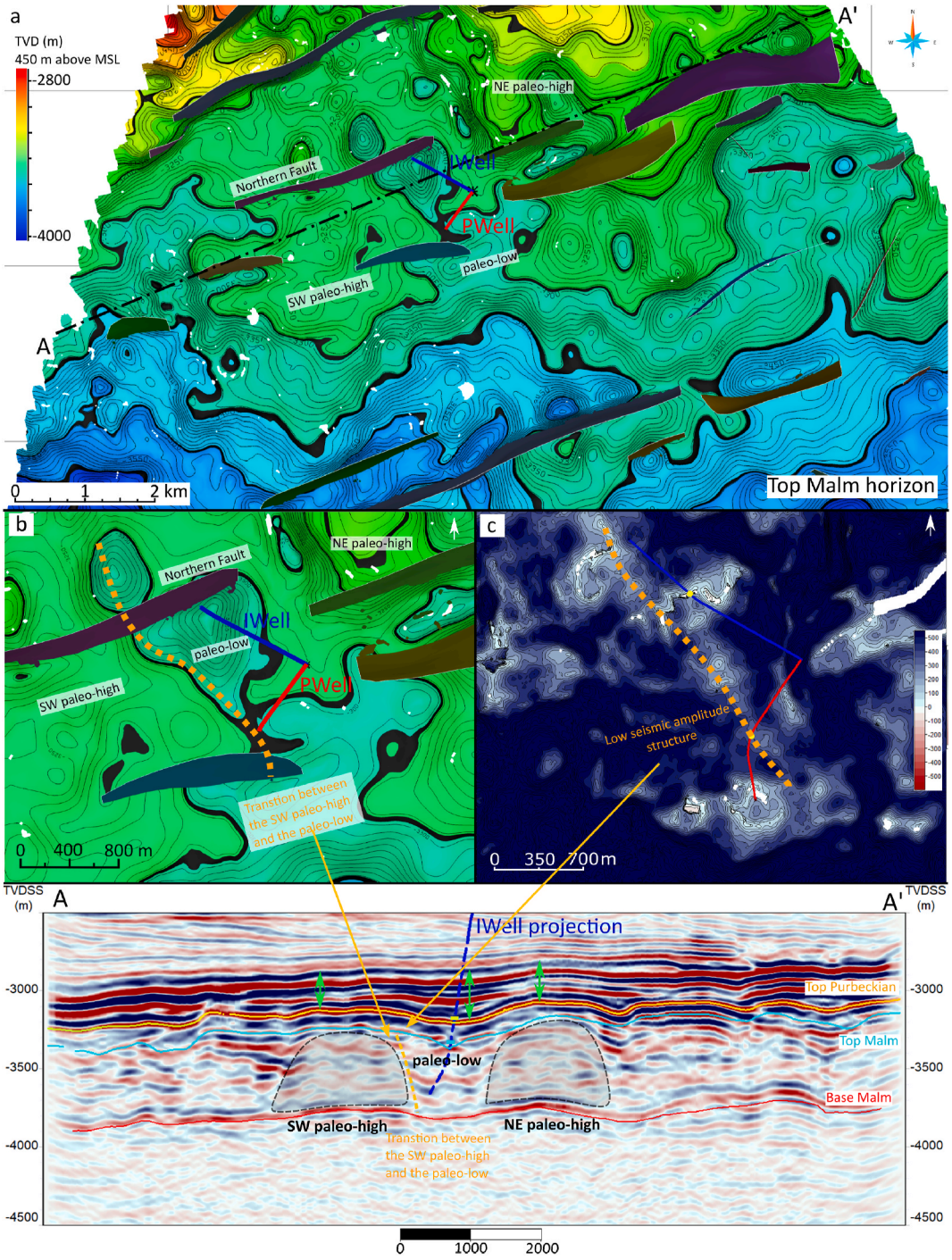

Fig. 3. Seismic scale structures around the wells (modified after Fadel et al., 2022). a) Top Malm horizon in depth domain delineating the change in the structural morphology of the Top Malm paleotopography. b) A zoomed-in map delineating the extent of the paleo-high at SW, the transitional zone (dashed in orange color), and the paleo-low (in the middle). c) Seismic amplitude attribute superimposition on Top Malm delineating a NW to NNW striking structure of low seismic amplitude at the location of the transitional zone between the paleo-high and paleo-low in b. The bottom panel is a depth seismic cross-section A-A′ (in a) displaying the morphology of the paleo-highs and the paleo-low including the embedded seismic amplitude signature.

penetrating a transitional zone between the SW paleo-high and its paleo-low at the NE (Fig. 3b). The cross-section A-A′ in Fig. 3 delineates the relative location of the paleo-highs with respect to the IWell projection. As shown in the cross-section A-A′, the paleo-highs accommodate chaotic seismic signatures, where the overlaying formations are thinning at their peaks. The paleo-low contains a relative increase in the seismic amplitude magnitudes, where the overlying formations are thickening. The paleo-high structures are interpreted as reefal buildups (massive facies); whereas the paleo-low in the middle is interpreted as lagoonal deposits (bedded facies). Similar interpretations to reefal buildups have been displayed by Chopra and Marfurt (2007), Fadel et al. (2021), Thomas et al. (2010), von Hartmann et al. (2012) and Wadas and von Hartmann (2022).

The well-to-well correlation in Fig. 4 shows that the lithology of the upper section of the IWell is dominated by limestone, where there is a high density of bedding planes dipping to the south. In contrast, the PWell is dominated by dolomite and lower beddings density of average dip direction towards the E to SE. The dominance of dolomite in the

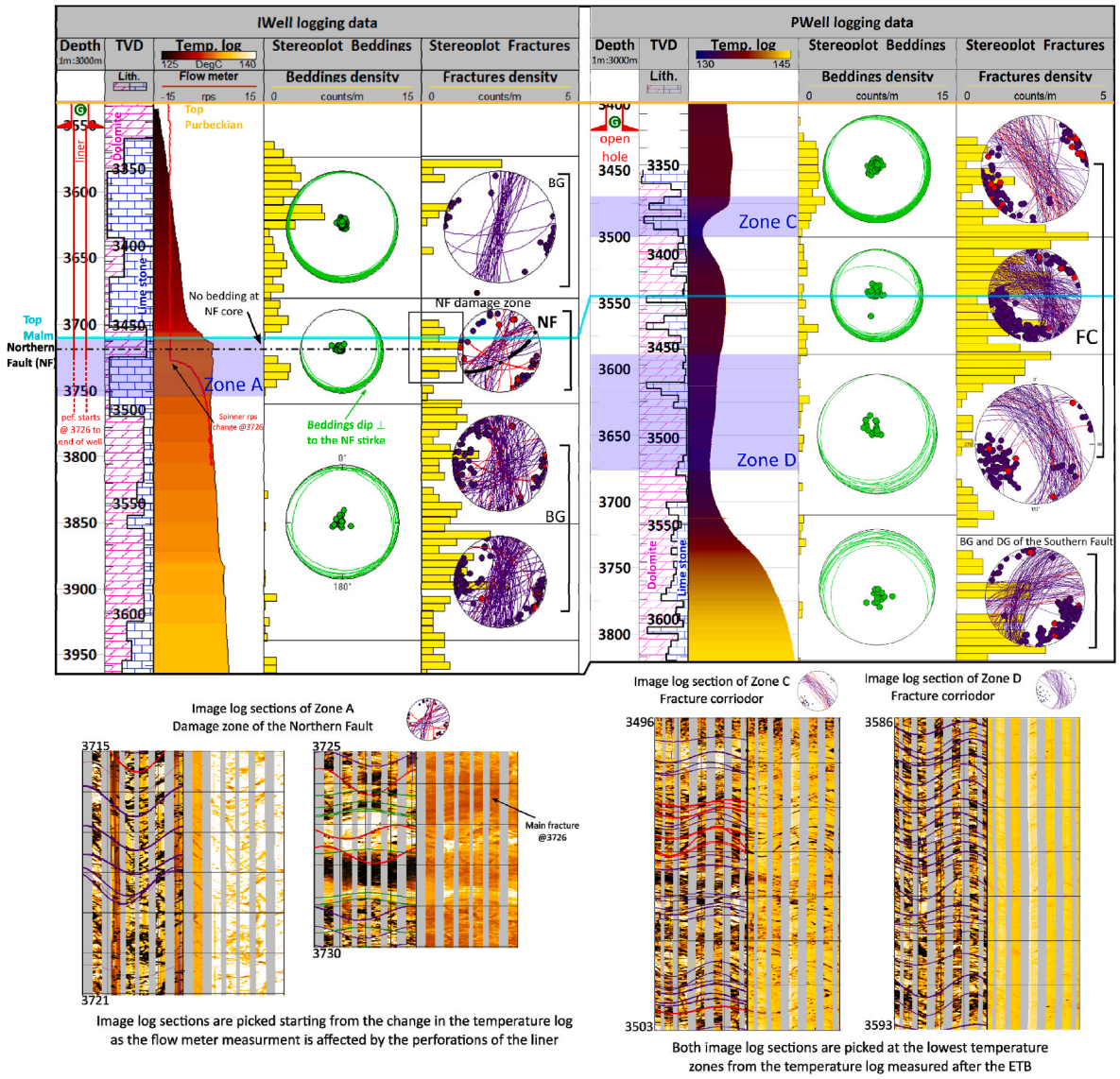

Fig. 4. Well to well correlation between the IWell and the PWell leveled at the Top Purbeckian (modified after Fadel et al., 2022). Main inflow zones (A, C, and D) interpreted from combing temperature and flow meter logs in the PWell and the IWell. We display the density (yellow bars) of the interpreted beddings (green) and the fractures (purple: partially open fracture, red: open fractures) as well as their stereographic plots (lower hemisphere) at depth intervals. The G sign represent the location of the pressure gauges used in well testing. Four different fracture sets were identified: two background (BG) fracture sets, the Northern Fault damage zone (NF) and the fracture corridor (FC) fracture sets. Lower panel displays resistivity image log sections of the inflow zones.

PWell is related to the improved fluid circulation provided by the high primary permeability of the interpreted reefal buildup (Bachmann et al., 1987; Bagrintseva, 2015; Dussel et al., 2016; Fadel et al., 2022). The lack of dolomitization in the IWell is related to the low primary permeability of the interpreted lagoonal facies existing in the vicinity of the IWell. The PWell is penetrating the flank of the reefal buildup, where the beddings (at the upper section of the reservoir) are steeper and dipping more to the east, reflecting the structural setting of the SW paleo-high shown in Fig. 3a and 3b.

2.3.2. *Fractures classification*

Fadel et al. (2022) interpreted 1591 fractures from the image logs of the PWell (1012 fracture) and the IWell (579 fractures), classified as partially open and open fractures. Moreover, the authors identified the location of the Northern Fault along the IWell and identified a fracture corridor in the PWell (Fig. 4). The following sections identify the influence of those structures on the location of the inflow zones interpreted from temperature and flow meter logs.

2.3.2.1. Northern Fault. Zone A is picked as the main inflow zone of the IWell based on combining the observations from the temperature log (convective zone) and the flowmeter log (change in the spinner rate per sec) (Fig. 4). The temperature log was measured before setting the perforated liner (GTN, 2010). After the ETB, the project owner preformed a flow meter log (shown in Fig. 4) to identify the exact location of injection (BRG, 2018a). The flow meter indicated that 100% of the well injectivity occurs in Zone A at 3726 m MD. As displayed in Fig. 4, the offset of the spinner is within the convective zone observed from the temperature log; however, the offsets of the curves are not coinciding due to the liner perforations, which start at 3726 m MD. We observe a fracture exactly at 3726 m MD, as displayed in the image log sections.

Zone A is the intersection zone between the IWell and the Northern Fault (Fig. 3a and 3b). The beddings density decreases from 7 to 3 bedding per m, where beddings are absent at the Northern Fault core. Moreover, the beddings dip orientation changes from S to SE, nearly perpendicular to the strike of the Northern Fault. On the other hand, the fracture density increases within Zone A, where the strike of the

fractures in that interval deflect towards NE, oblique to the strike of the Northern Fault (representation of the Northern Fault is labeled as NF in the stereo plot in Fig. 4). The thickness of the damage zone can be identified from the change in the fracture density. At the beginning of the damage zone, low density of fractures is observed, where a maximum is reached before the Northern Fault core, and a decrease in the fracture density is observed by the end of the damage zone. Mayolle et al. (2019) observed similar fracture density changes in a normal fault of 70 m throw. Based on these observations, the horizontal width of the Northern Fault damage is 30 m, and has the major influence on the IWell permeability. Fig. 4 displays image log sections for Zone A, which is dominated by high fracture density and low beddings density.

2.3.2.2. NNW fracture corridor. The temperature log of the PWell in Fig. 4 was measured after the occurrence of the thermal breakthrough (BRG, 2018b). Zones C and D are picked as the main inflow zones because they accommodate a lower temperature than the rest of formation temperature. This is due to the arrival of the cooled reinjected waters to the PWell (Fadel et al., 2022).

Zones C and D have fractures striking dominantly towards NW to NNW. The superimposition of the seismic amplitude attribute on the Top Malm horizon in Fig. 3c displays a low seismic amplitude structure striking NW to NNW. This sturcture stretches for 1500 m, bounded from the north by the Northern Fault, and has a width of 180 m, based on the lateral distance of the corridor from Fig. 4. This structure coincides with the transitional zone between the SW paleo-high and the paleo-low (Fig. 3b and 3c). Homuth et al. (2015) indicated from outcrop analog studies that transitional zones between reefal buildups and bedded facies accommodate high density of vertical fractures (Fig. 20). The described outcrop are considered by the same author as an analog of the Malm reservoir investigated in the present study. Fig. 4 displays image log sections for zones C and D, which accommodate high density of fractures striking NW.

The positive correlation between the strike of the transitional zone (Fig. 3b), the low seismic amplitude structure (Fig. 3c), and the local occurrence of high density sub-seismic fractures in zones C and D (Fig. 4), indicates that the sub-seismic fractures corresponds to a fracture corridor (Fadel et al., 2022). The fracture set of the fracture corridor is a result from the change of the structural morphology between the reefal buildup and the lagoonal facies and considered as burial fractures. Moreover, those fractures are critically oriented with the SHmax (N-S).

2.3.2.3. Background fractures. The rest of the fractures interpreted from the image logs are striking NNW, N-S, NNE, NE-SW, W-E and ENE-WSW. Those fractures reflect the tectonic history in the study area. The ENE-WSW and the W-E striking fractures correspond to the paleo-extensional regime (Bachmann et al., 1987; Freudenberger and Schwerd, 1996). The NNW, N-S, and the NNE fracture are interpreted as shear fractures reflecting the current compressional regime, where the SHamx is N-S (±20°) (Reinecker et al., 2010). The background fractures don't form large fracture networks as they are not correlated with large scale seismic structures to form permeable reservoirs.

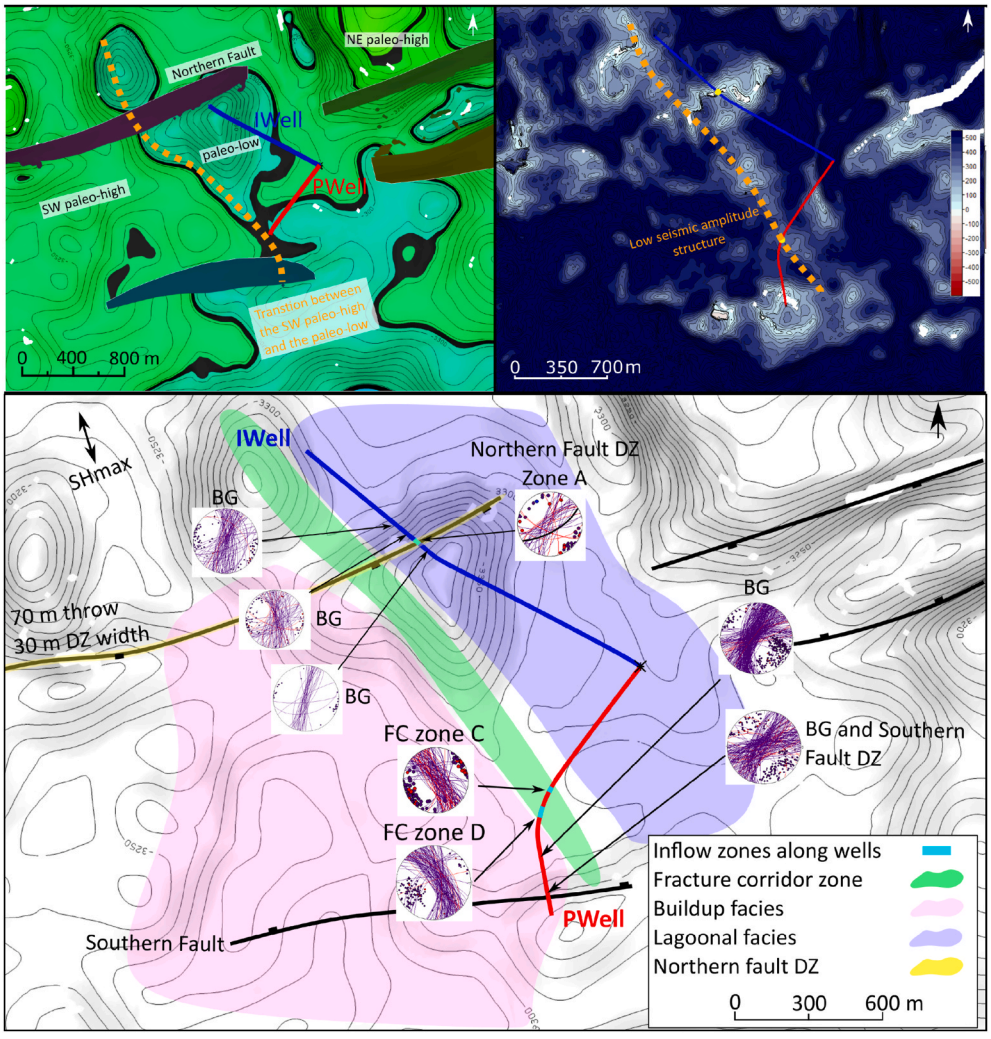

Fig. 5. Correlating seismic scale and sub-seismic scale interpretations on a map view to deduce a conceptual hydrogeological model of the reservoir at the study area (modified after Fadel et al., 2022). A positive correlation between the strike of the sub-seismic fractures, the low seismic amplitude structure, and the strike of the transitional zone postulates the existence of a fracture corridor (FC). The hydraulic communication between the two wells is due to the coupled fracture network between the Northern Fault damage zone (DZ) and the FC.

2.3.3. Conceptual hydrogeological model

Fadel et al. (2022) deduced a conceptual hydrogeological model shown in Fig. 5. The hydrogeological model suggests that the coupled fault damage zone and the fracture corridor constitutes the main elements controlling the reservoir permeability in the study area. Fluid circulation between the two wells occurs through the hydraulic communication of the fracture network between these structures. In addition, two background fracture sets striking N-S to NNE and W-E to ENE can be identified. The conceptual model constitutes our idealization of the permeability structure of the Malm reservoir at the study area. Hence, we utilize this information as a tool in constraining the PTA interpretations.

2.4. Overview and quality of the well testing data

Well test operations for the geothermal doublet were conducted through the utilization of downhole pressure gauges. The gauges for the PWell and the IWell were set at 3326 m TVD and 3309 m TVD, respectively (Fig. 4). During well testing, both wells had an open hole completion, where the production casing shoe for the PWell and the IWell were at 3327.5 m TVD and 3318.2 m TVD, respectively. The gauges were placed exactly at the top of the formation (Top Purbeckian), where the vertical distance between the gauges and the production casing shoe was 1.5 m TVD and 9.2 m TVD, for the PWell and the IWell, respectively (GTN, 2010, 2009).

Galvao et al. (2020) presented an equation to derive the maximum distance between the gauge and the perforations that allows the application of isothermal interpretation models. Using the latter formulation, we find that the maximum distance is 316 m and 661 m for the PWell and the IWell, respectively. Hence, applying isothermal interpretation models are viable within the framework of PTA. In addition to the optimum placement of the gauges directly above the top of the formation and the fact that we deal with buildup test evaluation, the influence of friction is negligible and has been discarded in this work (e.g., Saldana and Ramey, 1986). Other gauges were set to evaluate any pressure drift potential, where no drift was observed (GTN, 2010, 2009).

Fig. 6 displays the time span of the well testing operations performed in the IWell and the PWell. Acidization and well testing operations were applied first in the PWell. After several weeks, the IWell was acidized and tested, where reaction measurements were carried out in the PWell. Just before the interference test between the PWell and the IWell started, a circulation test in a nearby geothermal project (SW at 6.1 km away from the study area) was under operation for several weeks and ended before the start of the interference test (GTN, 2010). Hence, the reservoir pressure equilibrium was disturbed, and the initial measurments of the interference test is affected by an apparent increase in the reservoir pressure due to injection. In our PTA study, we included only the last buildup test as it would have the least effect from the possible reaction of the nearby interference.

The yellow-colored intervals in Fig. 6 indicate the timespan for cleaning and acidizing the PWell and the IWell. Red-colored intervals are corrupted or missing data. Green-colored intervals indicate the timespan of the last buildup test utilized in our study. As shown in Fig. 7, they are labeled as BU1, BU2, and BU3 for the PWell, the IWell, and the interference test, respectively. BU1 lasted for 30 hrs, BU2 lasted for 100 hrs, and BU3 lasted for 300 hrs. The long time of the buildup phase and the optimum gauge placement (at Top Purbeckian) enables the transient pressure radius of investigation to reflect all the expected responses including early: wellbore storage and skin, middle: reservoir behavior, and late times: reservoir boundaries.

3. Methodology

The main objective of this study is to define the reservoir system type, which can reflect the reservoir permeability structure and define its hydraulic behavior. Moreover, we investigate if it is possible to detect the influence of sub-seismic structures from the pressure response. This is done by simultaneously integrating the information in section 2.3 and analyzing the collected well testing data by applying the following workflow (Fig. 8):

1. Deriving the PD plots for each of the buildup tests
2. Interpreting the PD plots through the identification of characteristic flow regime type
3. Selecting interpretation models for the reservoir and the reservoir boundary sections
4. Deducing a conceptual reservoir model based on the interpretations
5. Solving and matching the interpretation models with the actual data
6. Deriving the hydraulic reservoir parameters
7. Utilizing the derived hydraulic reservoir parameters in numerical calculations to represent the geological complexity

3.1. Pressure derivative calculation

The analysis starts by deriving the PD for the three buildup tests (BU1, BU2, and BU3) shown in Fig. 7. The PD is the time rate of change of pressure during a test period and is described according to Bourdet

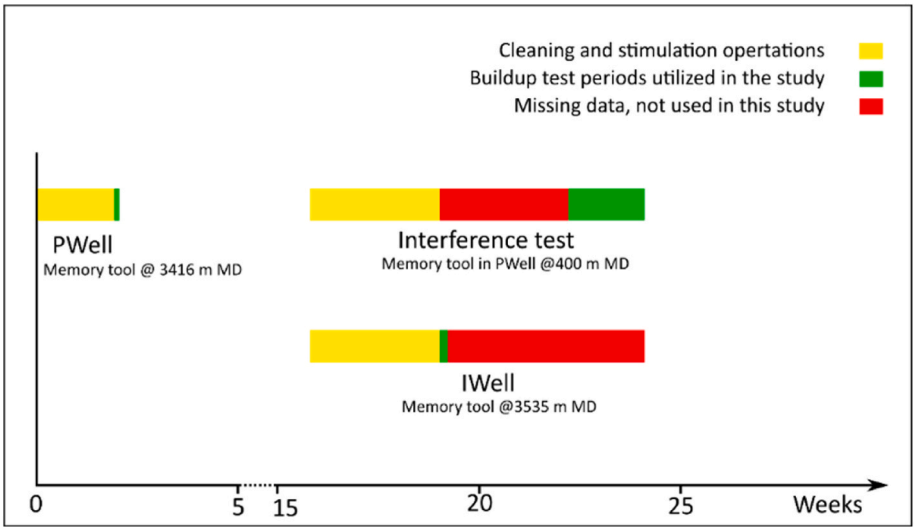

Fig. 6. Timeline of the well testing operations applied for the geothermal doublet.

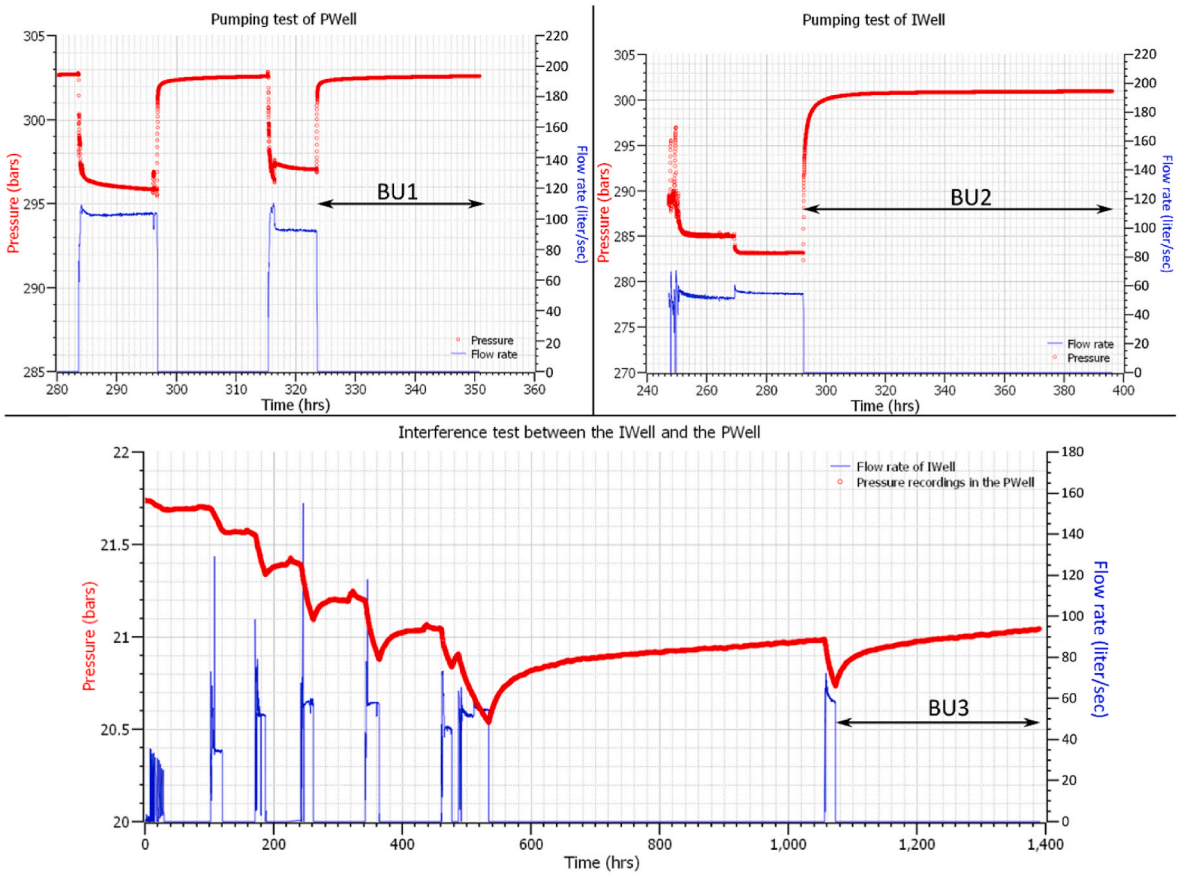

Fig. 7. Flow rate and pressure change plots of the geothermal doublet during well testing. BU1, BU2, and BU3 are the utilized buildup tests for the PWell, the IWell and the interference test, respectively. They are the final buildup tests after acidizing and cleaning.

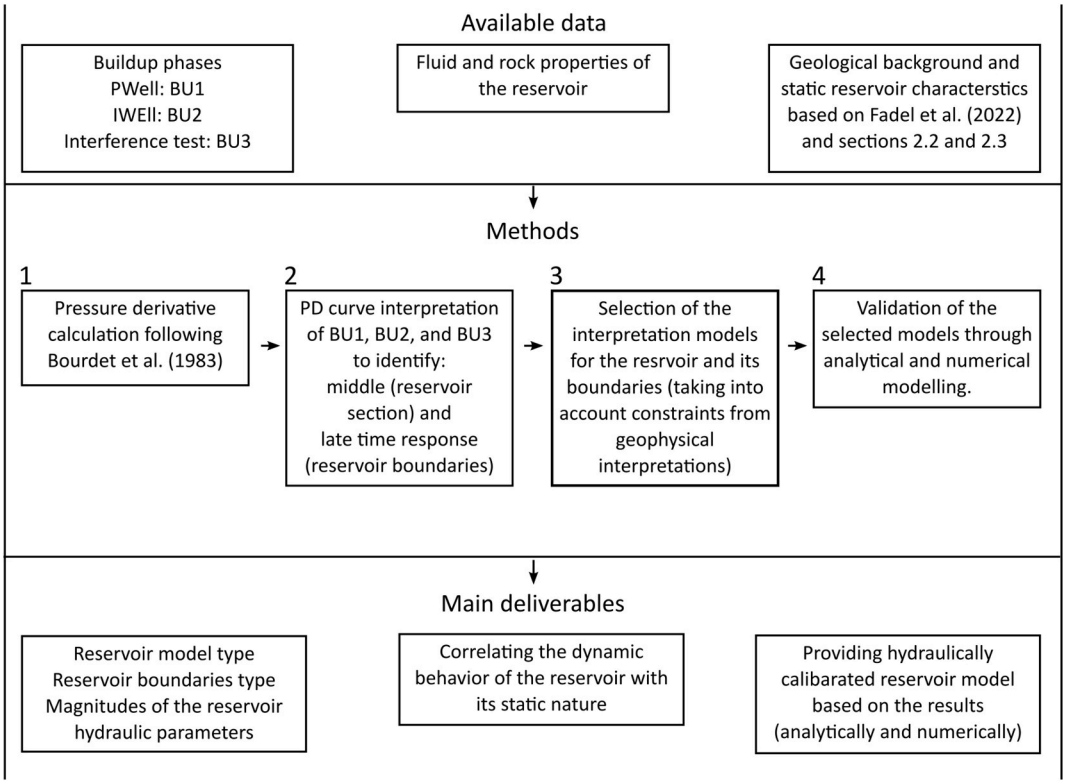

Fig. 8. Chart displaying the available data, methods, and the main deliverables of this study.

et al. (1983) by the following equation:

$$\Delta p' = \Delta t \frac{dp}{dt}$$

where $\Delta p'$ is the PD resulting from the multiplication of the elapsed time Δt since the beginning of the period by the pressure time derivative $\frac{dp}{dt}$. The PD is then plotted on log-log plot vs Δt. Smoothing is applied on the PD for the three buildup tests such that the smoothing coefficient magnitude (less than 0.2) does not mask important features of the buildup test or introduce distortions (Bourdet et al., 1983).

3.2. Interpretation of the PD plot

Distinct flow regimes and changes in the flow properties during buildup tests are identifiable through analyzing the PD plots. The PD is considered as a magnifying glass to the pressure difference behavior, where it helps characterize the flow regime type at different periods during the buildup test (Houzé et al., 2021). Ideally, it is possible to identify three different time periods on the PD plot:

- Early response corresponds to the wellbore storage/completion and the skin effect. The characteristic slope (m) of the PD curve for constant wellbore storage is 1 followed by a hump representing the skin effect. Early response lasts for variable times depending on the degree of the formation damage, fluid properties, wellbore completion, and the reservoir permeability (Bourdet et al., 1983).
- Middle response reflects the characteristic flow regime occurring in the reservoir. For homogeneous reservoirs, steady state radial flow is characterized by a straight line of m = 0. Reservoirs of multiple domain systems of different storativity cause a deviation from the radial flow stabilization due to reservoir heterogeneity. They form either a trough-shaped curve, which reflects a storativity increase (e.g., double porosity reservoirs), or a hump-shaped curve, which reflects a storativity decrease (e.g., composite reservoirs). The recognition of these changes can help in interpreting the reservoir system type from the PD plots (Bourdet, 2002).
- Late response corresponds to the acting reservoir boundaries. The buildup test needs to be long with optimum reservoir properties for the effect of the boundaries to appear unequivocally on the PD plots. Infinite acting reservoirs is characterized by a straight line of m = 0. If no-flow boundaries exist, there will be a change in the fluid mobility. The change in the mobility is described by a vertical displacement from the infinite acting reservoir stabilization. A positive slope PD straight line at the end of buildup tests usually reflects a decrease in the mobility due to the existence of no-flow boundaries (Djebbar and Anil, 1980; Wong et al., 1986).

3.3. Conceptual reservoir model

Based on the interpretation of the PD plots, interpretation models for middle and late time responses are selected. We simplify the early responses to be vertical wells of constant wellbore storage and skin because our study focuses on identifying the behavior of the reservoir and its boundaries, which ultimately controlled the occurrence of the ETB (Table 1). The selected interpretation models for middle and late time responses are then taken as a base for conceptualizing the reservoir setting at each well and for the whole reservoir. The conceptual model acts as a starting point for validating the selected interpretation models to match the actual buildup data.

Table 1 displays the magnitudes of the constant parameters for the reservoir/well settings for the matching process. We chose the reservoir net-thickness to be 200 m based on the results of Fadel et al. (2022); section 2.3. The fluid viscosity is derived based on the water properties at 302 bar and 140 °C (Wagner and Kretzschmar, 2008). The total reservoir compressibility is derived for the Malm reservoir carbonates according to (Pei et al., 2018). The Malm geothermal reservoir in the study area host low enthalpy geothermal resources, where temperature does not exceed 141 C° at the reservoir pressure (300 - 305 bar). Hence, single-phase flow models under confined conditions are considered. We set the average porosity magnitude of the reservoir to be 8%, according to core measurments taken from a nearby project (Bauer et al., 2021).

3.4. Validation of the interpretation models (analytically and numerically)

The interpretation models are analytical, transfer functions, representing models of the reservoir and its boundaries. To validate the selected interpretation models, the solution of the model functions should provide a good match with the actual pressure difference and the PD plots. If a good match is reached between the calculation of the selected interpretation models and the real data, in conjunction with evidences on the reservoir nature from geological and geophysical data, constraining the reservoir model type is likely unambiguous. A complete history match simulation for the interference test is also applied to validate the picked models and to obtain the final hydraulic parameters of the reservoir. However, it is hard to achieve a relationship between the parameters estimated from well test interpretations and the static measurements from core and logging data, since the well testing provides average magnitudes to the reservoir parameters. Accordingly, we apply 2D numerical reservoir modeling to simulate the interference test, based on the final derived hydraulic parameters from the matching process. The outcome will be considered as the basis for future robust long-term thermo-hydraulic modeling approach that we are currently investigating.

4. Results

4.1. Pressure derivative plots

4.1.1. PWell (BU1)

The log-log plot of the PD and the pressure difference of BU1 is displayed in Fig. 9. The total pressure difference throughout the buildup is around 5.5 bars after an average drawdown of 85 liter/sec. Based on the behavior of the PD, the plot could be divided into three responses.

Table 1
Input parameters for the matching process of the interpretation models.

	Well type	BU1 (PWell)	BU2 (IWell)	BU3 (Interference test)
		Vertical fully penetrating	Vertical fully penetrating	Observation point (source point)
Wellbore radius	*[Inch]*	4.25	4.25	4.25
Net reservoir thickness	*[m]*	200	200	200
Average reservoir pressure	*[bar]*	302	302	302
Reservoir temperature	*[°C]*	140°	140°	140°
Fluid viscosity	*[centipois]*	0.2169	0.2169	0.2169
Total reservoir compressibility	*[1/MPa]*	0.001029	0.001029	Deliverable from BU3
Matrix porosity	*[%]*	8	8	Deliverable from BU3
Distance between wells	*[m]*	0	0	1050

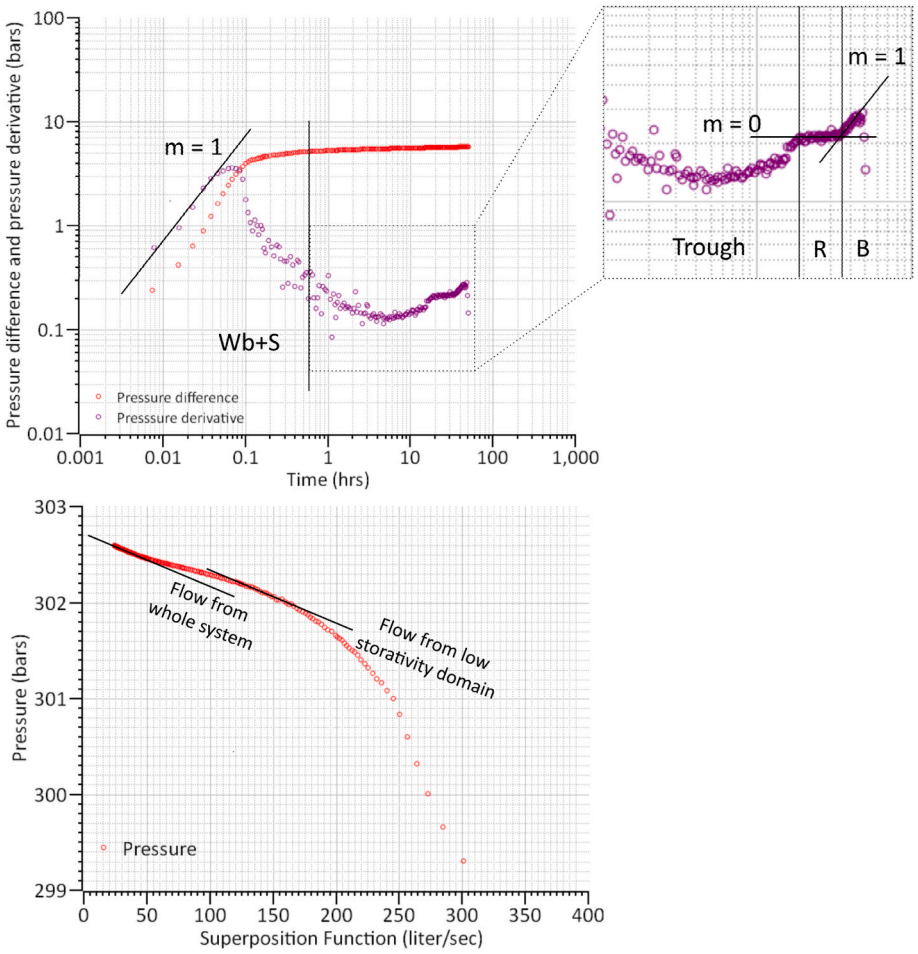

Fig. 9. Log-log (top) and superposition function (bottom) plots for the PWell-BU1. It is possible to distinguish early, middle, and late time interval responses in the log-log plot. A trough-shaped curve is observable from the upper graph and two parallel lines are possible to be drawn in the lower graph, indicating a double porosity or a layered system. (Wb + S: Wellbore storage and skin, R: Radial flow, B: Boundaries).

- Early response:

$t < 0.6$ hrs: This section represents the pressure response related to the effect of the wellbore storage ($m = 1$) and the skin (Wb + S). The PD plot starts with a straight line of $m = 1$, followed by a steep decrease in the derivative slope which is attributed to a changing wellbore storage. In the case of geothermal wells, this is attributed to the vertical change in the fluid temperature in the wellbore. This causes a change in the fluid column compressibility, causing a change in the wellbore storage. A -0.5 slope in the PD is observed afterwards representing a spherical flow. That indicates that the flow streamlines converge to the inflow-zone points.

- Middle response:
  a) $0.6 < t < 18$ hrs: The PD plot exhibits a trough shape representing an apparent decrease followed by an increase in the storativity. This behavior indicates that two domains exist in the reservoir system. This could be a result of a composite reservoir of variable porosity formation layers, or a fractured reservoir of double porosity behavior. In both systems, fluid flow is occurring first in the low storativity domain (high permeability layer or fractures) then from the whole system (low and high storativity domains).
  b) $18 < t < 35$ hrs: A PD line of $m = 0$ is observed for 17 hrs indicating a radial flow (R). The radial flow indicates that the fluid flow equilibrium is reached between the different porosity domains in the reservoir. Two parallel lines can be drawn in the superposition function curves displayed in Fig. 9, one representing the low storativity domain, and the other representing equilibrium of fluid flow of the whole system.
- Late response:

$t > 35$ hrs: For 10 h, the PD exhibits a vertical displacement from the radial flow stabilization, indicating a decrease in the fluid flow mobility. This reflects the influence of the reservoir boundaries on the PD indicating that the reservoir is not infinite acting.

4.1.2. IWell (BU2)

The PD and the pressure difference of BU2 are plotted on a log-log plot in Fig. 10. The total pressure difference is around 19 bars for a drawdown of 50 liter/sec. In comparison with BU1, the reservoir vicinity at the IWell has a lower transmissivity than the PWell. Despite the relatively long time of BU2 (100 hrs), we could only distinguish two time interval responses:

- Early response

$t < 1$ hrs (Fig. 10): This section represents the effect of the wellbore storage and the skin (Wb + S). The hump at 0.2 hrs is characteristic of phase segregation, possibly due to a gas pocket release. The buildup derivative curve stabilizes afterwards, indicating that the remaining data can be properly analyzed.

- Middle response

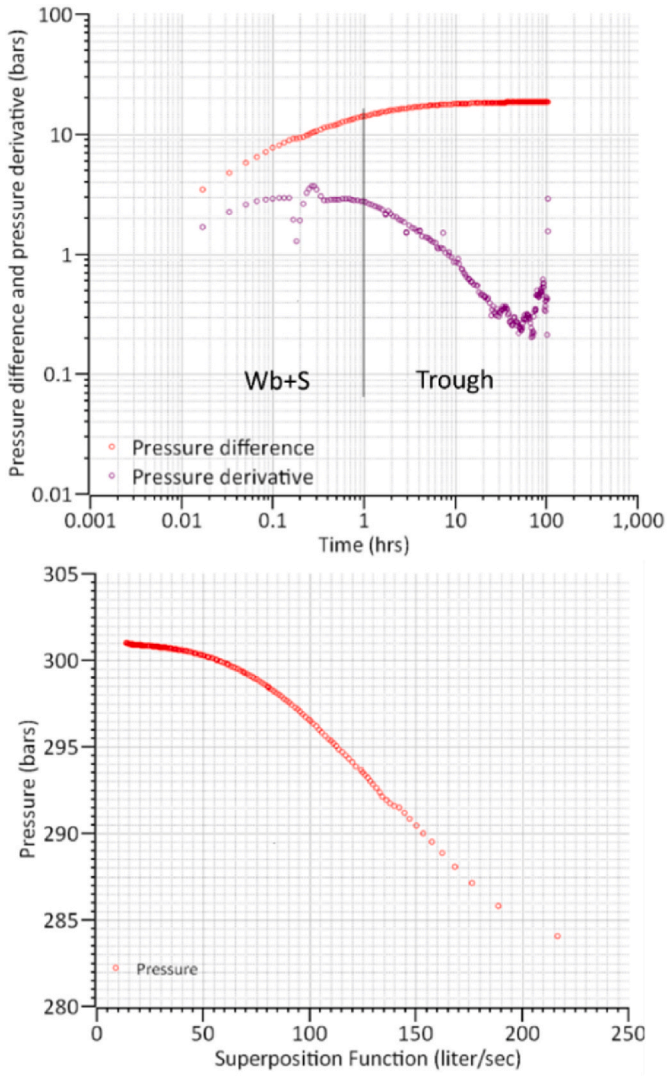

Fig. 10. Log-log (top) and superposition function (bottom) plots for the IWell-BU2. It is possible to distinguish only early and middle time intervals from the plots. Radial flow is missing in both plots, indicating that the system did not reach flow equilibrium between the reservoir domains. (Wb + S: Wellbore storage and skin).

t > 1 hrs: The PD plot exhibits a trough shape representing an apparent increase in the total storativity, similar to BU1. The trough in BU2 occurres later and is steeper in comparison with BU1. This behavior indicates a multiple domain system; however, the interconnectivity between the low and the high storativity domains is not well established as in BU1. Despite the longtime of the test, radial flow was not achieved in the whole test. For the superposition function curve two parallel lines cannot be drawn.

4.1.3. Interference test (BU3)

For homogeneous reservoirs, the pressure response at the observation well (in interference tests) changes slowly with respect to the flow period in the active well (Bourdet, 2002). The time taken by the pressure transient wave to reach the observation well is dependent on the distance between the wells and the reservoir hydraulic properties. Bourdet (2002) indicated that the interference response occurs faster in fissured reservoirs than in homogeneous reservoir systems, as the fractures have very high permeability.

The interference test between the IWell and the PWell in Fig. 7 shows a very interesting behavior. Despite the 1050 m distance between the wells, the pressure response observed at the PWell changes almost immediately to the flowing period in the IWell. Moreover, it is clear that after long buildup times (for almost 500 hrs buildup) the reservoir pressure does not get back to its initial magnitude. Those observations indicate:

- There is an excellent hydraulic communication between the two wells, as the pressure in the PWell changes immediately.
- The incapability of the reservoir to get back to its initial pressure magnitude is likely due to the existence of multiple domains of different hydraulic properties (storativity and permeability).
- The existence of no flowing reservoir boundaries.

The log-log and the superposition function for BU3 in Fig. 11 displays the early and middle responses. Early time is dominated by a PD line of m = 0.5 for around 45 hrs. 0.5 slope lines is characteristic to linear flow regime. The late response of the interference test exhibits a PD line of m = 1. The vertical displacement of the PD curves at the end of the test indicates a mobility decrease, which is also observed in BU1 (Fig. 9).

Hence, we postulate that the low storativity/high permeability domain in the reservoir is responsible for the instant change in the pressure at the observation well, where the reservoir boundaries act as a resistive element to the buildup process of the reservoir pressure.

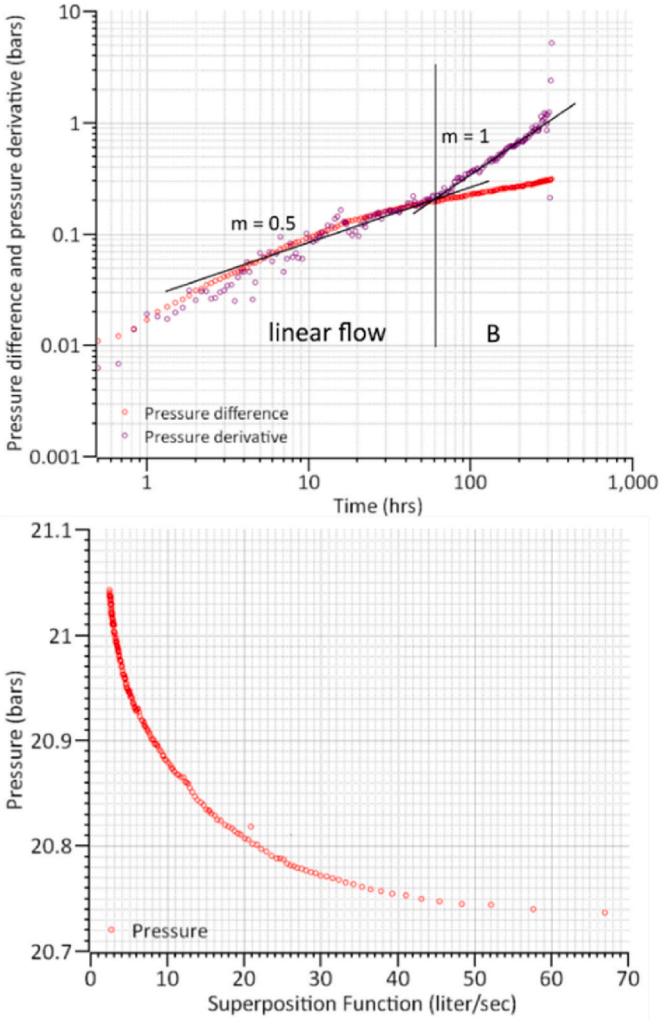

Fig. 11. Log-log (top) and superposition function (bottom) plots for the interference test between the IWell and the PWell (BU3). Linear flow dominates the initial stage of the test. The boundaries influence on the PD starts at t = 45 hrs with a line of slope = 1 in the log-log plot. (B: Boundaries).

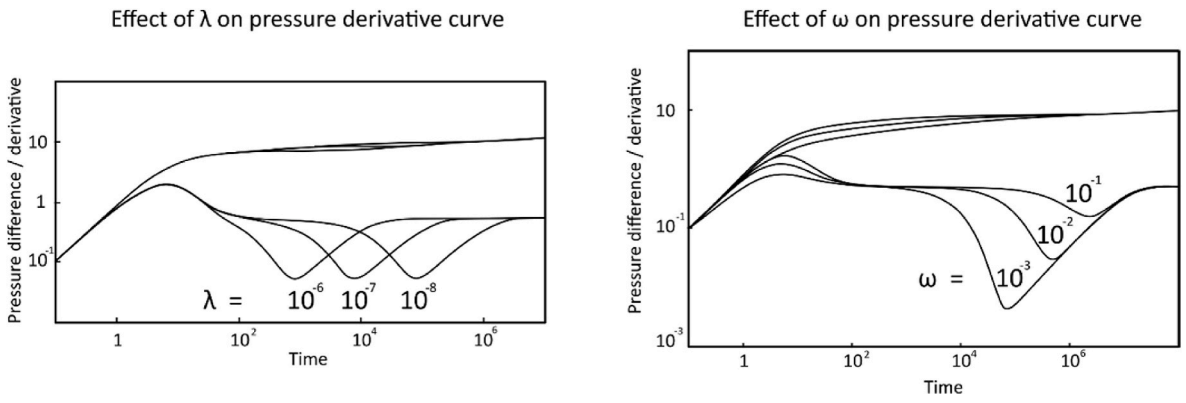

Fig. 12. Examples illustrating the influence of ω and λ on the PD (modified after Bourdet, 2002).

4.2. Interpretation of results

4.2.1. Reservoir permeability between the PWell and the IWell

The resultant pressure difference observed from the buildup tests reflects the productivity index magnitudes of the wells. Even though the drawdown rate for BU1 (average 90 liter/sec in the PWell) is higher than BU2 (average 55 liter/sec in the IWell), the total pressure difference in the PWell (5.5 bars) is lower than the IWell (19 bars) (Figs. 9 and 10). Accordingly, the productivity/injectivity index (as the fluid properties and the total reservoir thickness are the same) of the PWell is higher than in the IWell. This matches the interpretations in Section 2.3 (Figs. 3 and 4), where the PWell accommodates high fractures density and favorable facies type unlike the IWell.

4.2.2. Reservoir type

1) The PD plots of BU1 and BU2 during the middle time response exhibit a trough shaped curve, indicating a double domain system.
2) The dominant occurrence of fractures in the inflow zones (A, C and D) and their relevant location (A in Top Malm, C in middle Purbeckian, and D below Top Malm by 50 m) in Fig. 4, dismisses the possibility that the reservoir is layered (Fadel et al., 2022). If layering dominates, inflow zones would occur within the same stratigraphic formation. Moreover, the inflow zones in both wells are hydraulically interconnected indicating that beddings can not be laterally correlated between the two wells. Otherwise, a permeable zone would be located in the Purbeckican in the IWell or at Top Malm Zeta at the PWell.
3) The geophysical data interpretation in section 2.3 delineates the existence of a fracture corridor of NNW direction in the vicinity of the PWell, while the main inflow zone in the IWell is dominated by the Northern Fault damage zone.

Based on 1), 2), and 3) we interpret the reservoir to be naturally fractured. Fractures are the low storativity/high permeability domain, while the matrix is the high storativity/low permeability domain. Moreover, the observed dominant linear flow for 45 hrs during BU3 reflects the influence of the fracture corridor on the reservoir hydraulics.

The best fitting analytical interpretation model matching the middle response is a double porosity with restricted interporosity reservoir model. Pioneering works analytically describing reservoirs of double porosity behavior has been documented in Barenblatt et al. (1960) and Warren and Root (1963). They assume that naturally fractured reservoir is composed of two intercommunicating systems in one continuum domain, one of high storage capacity (matrix) and the other of high flowing capacity (fractures). Both systems are coupled with a transfer function describing the pressure gradient occurring between the fractures and the matrix due to production or injection. Fractures in this system are not discretely described; hence, the geometric influence of the fractures on the fluid flow (anisotropy) is overlooked. Since analytical models for clustered fractures are difficult to obtain, we utilize the dual porosity reservoir model initially proposed by Warren and Root (1963) for matching the data, to derive meaningful average reservoir parameters.

The main parameters describing the hydraulic behavior of double porosity reservoir models are the storativity ratio (ω) and the interporosity flow coefficient (λ) (Warren and Root, 1963). ω describes the contribution of the fracture system to the total storativity, while λ describes the ability of the matrix blocks to support fluid into the fractures. The equations for the two variables are:

$$\lambda = \alpha r_w^2 \frac{k_m}{k_f}, \omega = \frac{\varphi_f c_f}{\varphi_f c_f + \varphi_m c_m},$$

where r_w , k_m , and k_f are well radius, matrix permeability, and fracture permeability, respectively. α, φ_f, φ_m, c_f, and c_m are shape factor, fracture porosity, matrix porosity, fracture compressibility, and matrix compressibility, respectively.

As displayed in Fig. 12, changing the ω and λ magnitudes affects the shape of the trough-shaped curve. On the one hand, shallower troughs reflect larger magnitudes of ω indicating short transitional regimes between the fracture and the matrix domains. On the other hand, λ controls the time when the minimum of the trough occurs. Large λ magnitudes imply that the minimum of the trough occurs at earlier times than small λ magnitudes. Well-established interconnectivity between the matrix and the fractures reflects large λ magnitudes, while poor hydraulic connection between the matrix and the fractures is attributed to small λ magnitudes.

By graphically comparing the location of the ω and λ in both BU1's and BU2's PD plots (Figs. 9 and 10), we can observe:

1. The depth of the trough in the PWell is shallower than the IWell. Hence, ω in BU1 > BU2.
2. The time at which the minimum of the trough occurs in BU1 is at t = 4 h, while it occurs at t = 40 hrs in BU2. Hence, the λ of BU1 < λ of BU2.

We can deduce from the PTA that the interconnectivity between the matrix blocks and the fracture system in the reservoir section targeted by the PWell is better established than that crossed by the IWell. The fracture count at the location of the inflow zones (A, C, and D) in both wells are very different (Fig. 4). Zone A has 34 fractures, while Zones C and D have 183 fractures. Hence, we can correlate the low fracture density in the IWell with the late trough occurance in BU2. On the other hand, the high fracture density in the PWell results in an early occurrence of the trough in BU1. Hence, the PTA interpretations match the geophysical data interpretations.

4.2.3. Reservoir boundaries

Based on the behavior of the late times in BU1 and BU3, we select a channel boundary model to represent the late time response. The PD curve exhibits a straight line of m = 0.5 to 1 at the end of BU1 and BU3 indicating a decrease in the fluid mobility, which can result from two sealing parallel faults (Bourdet, 2002). Another indication for the decrease of fluid mobility can be observed from the raw data related to the interference test displayed in Fig. 7. The reservoir pressure is not capable of recovering its initial magnitude after long buildup times.

As mentioned in section 2.2, the reservoir lies in a graben structure and it is delimited from north and south by the Northern Fault and the Southern Fault Inventories, respectively. Both lineaments accommodate faults of throw nearly larger than the thickness of the upper section of the Malm (Malm Zeta), which exhibits the highest permeability. Both systems can induce seal juxtaposition across the faults plane and act as hydraulic barriers to fluid flow perpendicular to the fault plane.

Another explanation for the channel boundary behavior is the influence of the fracture corridor interpreted in Fig. 5. It can reflect a linear flow regime followed by a channel boundary effect at late times on the PD plots. The existence of the geothermal doublet in the graben structure or the presence of the fracture corridor can be a reason for the observed channel boundaries from the well test data analysis.

4.3. Reservoir conceptual model

Based on our interpretations from the PD plots in the previous section, Fig. 13 displays the deduced conceptual model representing a simplification to the reservoir setting. The model is divided into three parts:

1. Reservoir behavior around the vicinity of the PWell based on BU1.
2. Reservoir behavior around the vicinity of the IWell based on BU2.
3. Total reservoir behavior from the interference test BU3.

To properly compare the hydraulic behavior of the three parts, we apply the same assumptions (interpretation models) and the same petrophysical/fluid properties (Table 1) in our calculations. The following are the selected interpretation models for early, middle, and late time responses for each of the three parts:

- Fully penetrating vertical well of constant wellbore storage and skin for the early time in BU1 and BU2 (Bourdet et al., 1983).
- A point source (no skin or wellbore storage) for the early time of the observation well (PWell) in BU3.
- Double porosity behavior, with restricted interporosity flow model for the middle time response of BU1, BU2 (Bourdet and Gringarten, 1980; Mavor and Cinco-Ley, 1979), and BU3 (Bourdet and Gringarten, 1980; Deruyck et al., 1982).
- A channel boundary (two parallel sealing barriers, where the distance between them and the observation well are d_1 and d_3; Fig. 13) model for the late time response of BU1, BU2, and BU3 (Miller Frank, 1962; Nutakki and Mattar, 1982; Wong et al., 1986). The distance between the PWell and the IWell is 1050 m, where the angle of observation is 90°.

The variable parameters for each of the three parts in Fig. 13 are the permeability and the storativity ratios between the matrix and the fractures. Achieving a match between the results of the interpretation models and the real data under those conditions will validate our interpretations and can help in comparing the hydraulic behavior of the three reservoir parts shown in Fig. 13.

4.4. Matching the interpretation models

Fig. 14 summarizes all the matching plots for the three buildup tests based on the selected interpretation models in the previous sections. A good match for the middle and late times has been achieved for BU1, BU2, and BU3. There is a slight mismatch at the beginning of each test as the chosen models did not take into account the well deviation.

Fig. 15 displays the final history match for the whole buildup tests based on the derived parameters from the match. We utilized averaged step production rates for simplification. The history match conducted on the well test data of the PWell and the IWell shows comparatively good results. There is a good match at the end of the history test of the interference test. The initial mismatch is related to the interference from a nearby injection test, reflecting an apparent increase in the reservoir pressure.

The reservoir parameters derived from the matching process are listed in Table 2. We observe that the reservoir permeability in the vicinity of the PWell is ten times the IWell. ω and λ derived from BU1 (PWell) are also higher than the values determined from the BU2 (IWell). If the reservoir is layered and its permeability can be averaged, the magnitudes of the permeability, ω, and λ between the two wells would be close in magnitudes to each other. The large difference in the parameters magnitudes between the two wells is attributed to the relative location of the wells with the reservoir structural permeability. The PWell is penetrating a fracture corridor, where the total interpreted fractures in Zones C and D are 183 fractures (width 180 m). Whereas,

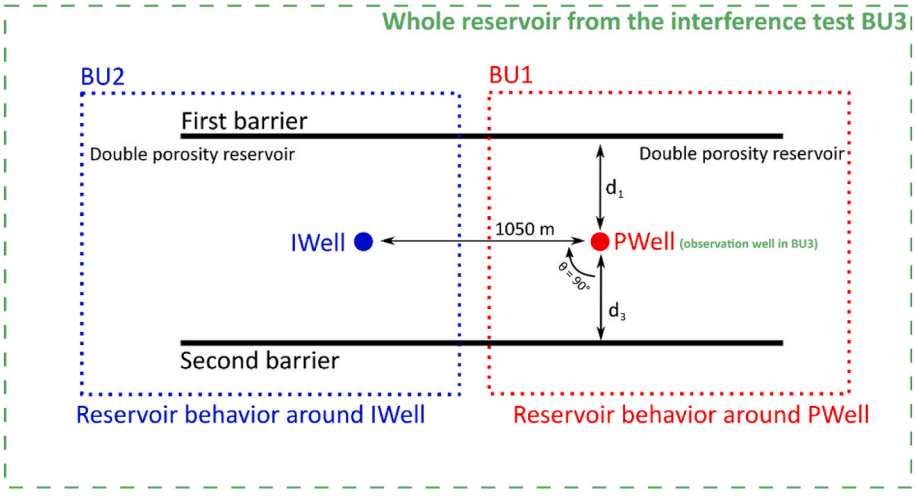

Fig. 13. Conceptualizing the reservoir system based on interpreting the PD plots of BU1, BU2, and BU3. We apply the same interpretation models and the same variables to the three reservoir sections to achieve a match with the real data of the buildup tests.

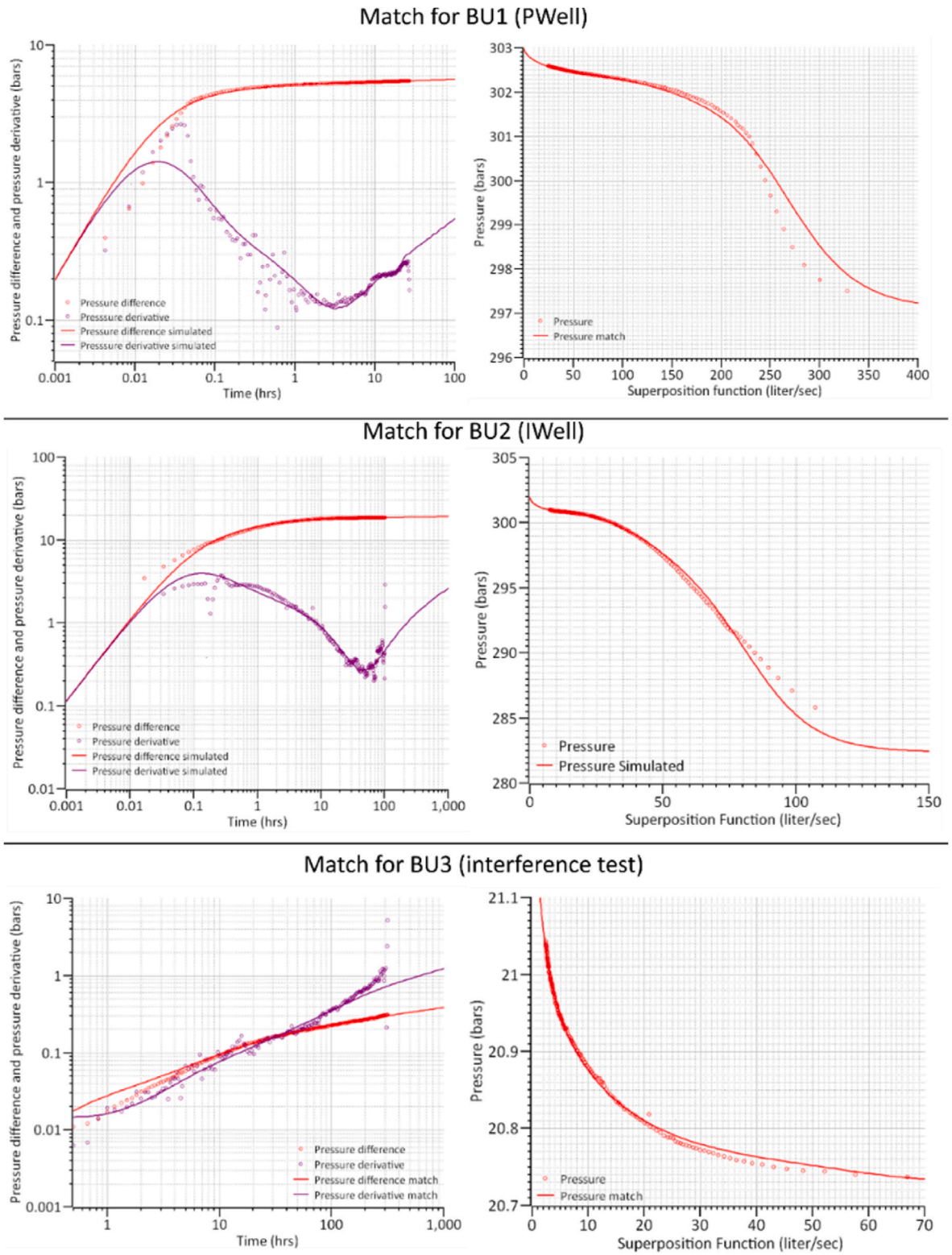

Fig. 14. Matching the selected interpretation models (simulated represented by lines) with the real data (represented by points) of BU1 (PWell), BU2 (IWell), and BU3 (Interference test).

Zone A in the IWell contains 34 fractures (width 30 m). We suggest that the change in the fractures density and the associated structures cause the difference in the hydraulic properties of the reservoir between the vicinities of both well.

The permeability derived from the interference test represents the overall average permeability of the reservoir. The high permeability of the whole reservoir indicates an excellent hydraulic communication between the PWell and the IWell. This high permeability is attributed to the linear flow exhibited by the fracture corridor coupled with the Northern Fault damage zone (Figs. 11 and 5). The magnitudes of λ and ω obtained in the interference test evaluation indicate that the reservoir is within the range of a naturally fractured reservoir: $0.01 < \omega < 0.001$ and

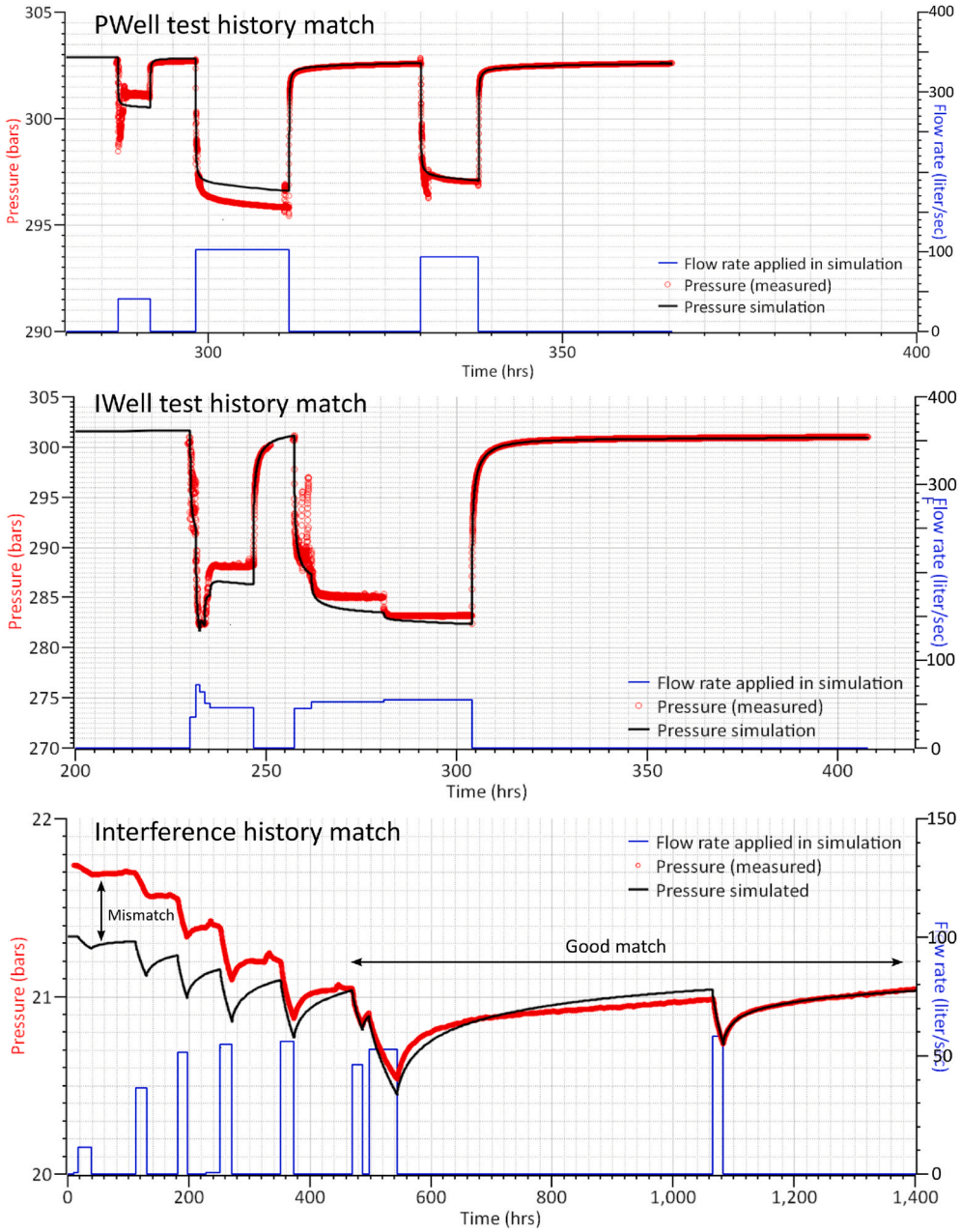

Fig. 15. Pressure history match for the derived parameters and the selected interpretation models from BU1, BU2, and BU3. The applied flowrates are averaged for simplification.

10E–4 < λ < 10E-10.

Another important deliverable is the lateral distance of the sealing boundaries with respect to the wells location. As shown in Table 2, d1 and d3 are 1500 m. Hence, the dynamic behavior of the reservoir can be represented by an isotropic fractured reservoir, which is bounded by two no-flow sealing boundaries, where the total width of the reservoir is 3000 m (conceptual model in Fig. 13).

The influence of the fracture corridor on the reservoir boundary response is not possible to be resolved using analytical solutions. This problem can be investigated utilizing numerical modeling to investigate if a coupled fracture corridor with a fault damage zone model would behave similarly to the conceptual model in Fig. 13.

4.5. Numerical calculation utilizing simplified discreet fracture network

In this section, we present a hydraulic simulation of the interference test between the IWell and the PWell based on the application of a fit-for-purpose 2D numerical modeling utilizing the Subsurface Flow Module of COMSOL Multiphysics®. We confirmed that the conceptual model - built based on the selected interpretation models - shown in Fig. 13 can match the pressure response of BU1, BU2, and BU3. However, the conceptual model does not represent the geological setting of the reservoir (section 2.3). The aim of the numerical model is to illustrate if it is possible that a discreet fracture network (DFN) representing the coupled damage zone and the fracture corridor can induce similar hydraulic behavior to the matched analytical model in Fig. 15. Achieving a match will illustrate the non-uniqueness nature of dynamic reservoir models and will support our interpretations in section 2.3.

4.5.1. Numerical reservoir model setup and parameterization

We set the dimension of the reservoir to be 8 km × 7.2 km, so that the pressure wave front does not reach the model boundaries during the

Table 2
Derived parameters from the matching of the interpretation models with BU1, BU2, and BU3, taking into account the conceptual model in Fig. 5 and the constants listed in Table 1. d1 and d3 are the distances from the wells to the sealing boundaries in Fig. 13, respectively.

		PWell reservoir vicinity (BU1)	IWell reservoir vicinity (BU2)	Interference test (Whole Reservoir BU3)
Permeability	*[mD]*	263	20	1089
ω	*Unitless*	1.90E-01	4.70E-02	9.50E-03
λ	*Unitless*	2.20E-08	1.28E-08	9.00E-09
Matrix specific storativity	*[1/Mpa)*	*NA*	*NA*	1.56E-03
Fracture specific storativity	*[1/Mpa)*	*NA*	*NA*	1.50E-05
Total storativity	*[m/Mpa)*	*NA*	*NA*	0.3147
d1	*[m]*	1500	1500	1500
d3	*[m]*	1500	1500	1500
Observation angle	*[°]*	*NA*	*NA*	90
Productivity index	*[liter/sec/bar]*	15.73	2.80	*NA*

simulation time (interference test duration). To achieve that, we conducted previous boundary-independence studies. We extracted the areal extent of the Northern Fault damage zone and the fracture corridor shown in Fig. 5 and used them as our areal constraints, filling them with vertical discrete fractures (Fig. 16a and b). The strike of the discrete fractures in the Northern Fault and the fracture corridor boundaries follows the strike of the fractures in Zones A (ENE) and C/D (NW) in Figs. 4 and 5, respectively (Fig. 16b). We set the fracture density in the fracture corridor to be double that of the Northern Fault damage zone. The reservoir domain is a porous medium of low permeability and high storativity compared with the discrete fractures. We consider a single-phase fluid flow in the matrix and the discreet fractures following Darcy's law under confined conditions. The reservoir system is a dual-porosity reservoir where the groundwater flow formulation describing the space and time dependent balance equations between the fractures and the matrix is illustrated in the Appendix.

For parametrization, we utilize the magnitudes of the hydraulic parameters derived from matching the interference test. Hence, we set up the numerical model to have similar parameter magnitudes to the ones in Tables 1 and 2. Our approach is to vary the matrix permeability and the aperture of the fractures - taking into account maximum and minimum matrix permeability magnitudes of the Malm reservoir from Bohnsack et al. (2020) and Homuth et al. (2015) - to achieve a match with the analytical model pressure response. The initial pressure is set to 21.34 bars as the measurments were taken by a shallow guage. In the numerical model, the IWell is set to be the operating well (production) and the PWell as the observation well (Fig. 16a). Furthermore, we utilize the same flowrate applied in the analytical model calculation.

COMSOL Multiphysics® applies the FEM in solving the system's partial differential equations. We utilize unstructured triangular mesh type in the model, where the maximum mesh size is set to be 200 m (Fig. 16c). We refine the mesh around the operating well and the discrete fractures, such that, the maximum mesh size around the IWell and the discrete fractures is 1 m and 3 m, respectively. The maximum element growth rate is set to 1.2 for a proper gradual increase of the mesh from the discrete fractures to the reservoir boundaries. The total number of the mesh vertices is 32,100, which includes 64,046 triangular elements. We apply a time dependent study as we investigate an unsteady state case, utilizing the Multifrontal Massively Parallel Sparse Direct Solver. The discretized diffusivity equations for the pressure (variable) is solved utilizing Lagrange quadratic shape functions.

4.5.2. Results, uncertainty, and conclusions

Fig. 16d displays a comparison between the resultant pressure decline (at the PWell) of the interference test calculated analytically and numerically. The numerical model pressure response matches the analytical one by combining 11.5 mD matrix permeability and 1.9 mm fractures aperture. Karstification processes together with the orientation of the fractures with respect to the current stress field may explain the relatively high fracture aperture. Furthermore, the match between the two models is a perfect example to the non-uniqueness problem of dynamic reservoir models. The results of the numerical model corroborate the fracture corridor existence. This explains the excellent hydraulic communication between the PWell and the IWell, which resulted in the early thermal breakthrough.

The DFN model in Fig. 16b is a simplified representation of the whole fracture system between the two wells. Other iterations of DFN models (different fractures length, density, connectivity; however, following the same overall orientation) can achieve a match by varying the matrix permeability and the fractures apertures (model uncertainty).

The time steps figures displayed in Fig. 16e illustrate the first drawdown and buildup phases marked in green in Fig. 16d. During the drawdown period, the pressure decline occurs first in the fracture corridor and then propagates into the matrix surrounding the discrete fractures. The reservoir pressure at the observation well (PWell) declines almost instantly because the factures have high permeability and low storativity and are depleted first before the surrounding matrix. We also observe the inability of the reservoir to recover its initial pressure during the buildup phase. The existence of the fractures and the matrix in the reservoir causes a high hydraulic resistivity to fluid flow in the reservoir system, which decelerates the buildup process. This causes a decrease in the fluid mobility, which is observed from the PD plots in BU1 and BU3. To visualize the whole interference test from the numerical model, we have supported our paper with a video displaying the spatial pressure evolution during the interference test in Appendix A Supplementary data.

5. Discussion

5.1. Acidization influence on the PD

Acidization is commonly applied in deep geothermal wells in the GMA, where it enhances the interconnectivity between the wellbore and the producing formation by removing any induced formation damage after drilling. Usually, acidization in the Malm reservoir is followed by wellbore cleaning and a buildup test to assess the productivity/injectivity enhancement of the well. Kikani and Walkup (1991) showed that changes in the PD curves can occur after acid stimulation in a fractured reservoir. The authors recognized an enhancement in the permeability of the producing formation associated with changes in the flow regime at middle response. In this section, we display a comparison between the behavior of the PD plots after acidization with the final PD plots of BU1 and BU2 (Fig. 17). Changes occur in the plots can provide insights on the reservoir system type and strengthen the PTA interpretations. Observing these changes show the progression of removing the formation damage, which decreases the pressure loss around the wellbore, allowing the pressure wave to propagate deeply into the reservoir reflecting its type.

Our first observation from Fig. 17 is that there is a similarity in the PD curve shape after first cleaning between the IWell and the PWell. Both PD plots end with a straight line of $m = -1$, indicating a constant pressure boundary or an infinite conductive fault. After acidization, the PD curves of both wells exhibit changes in their shape. Trough curves start to develop, indicating an increase in the storativity due to the double porosity system in the reservoir. It is also observable that ω and λ are directly proportional to the applied acidization operations. The apparent magnitudes for ω and λ become higher after acidization, indicating a development in the connectivity between the stimulated matrix and the fractures around the well. The magnitudes for ω and λ in

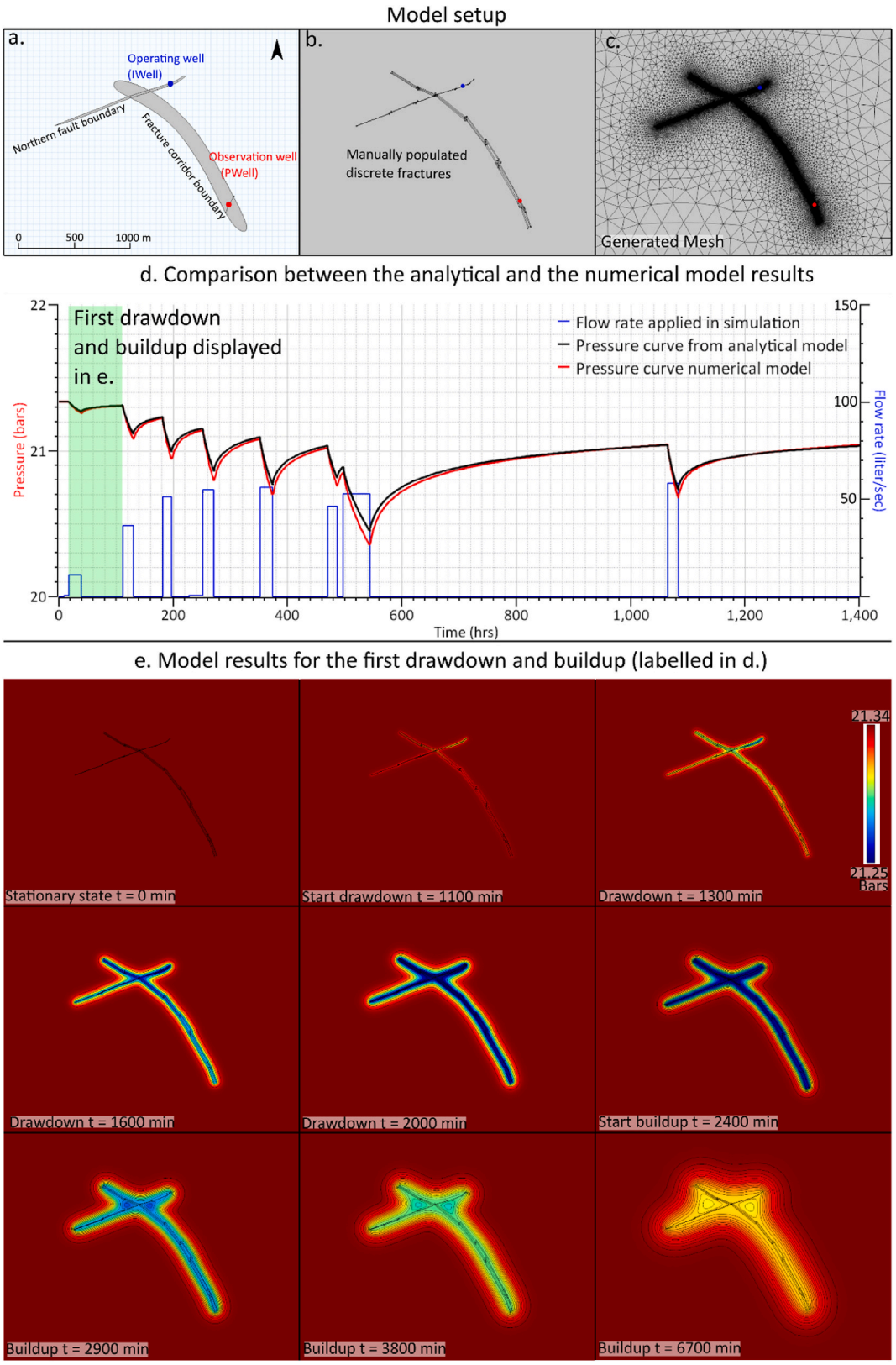

Fig. 16. The model set up and the results of numerically simulating the hydraulic interference test between the IWell and the PWell. a, b, and c are the steps followed in building up the model. d displays a comparison between the calculated pressure response from the analytical (in Fig. 15) and the numerical model. e displays a 2D spatial distribution of the pressure due the first drawdown and buildup test labeled in green in d. Notice the difficulty of the reservoir to recover its initial pressure due to the existence of two domains (fractures and matrix) of different hydraulic properties.

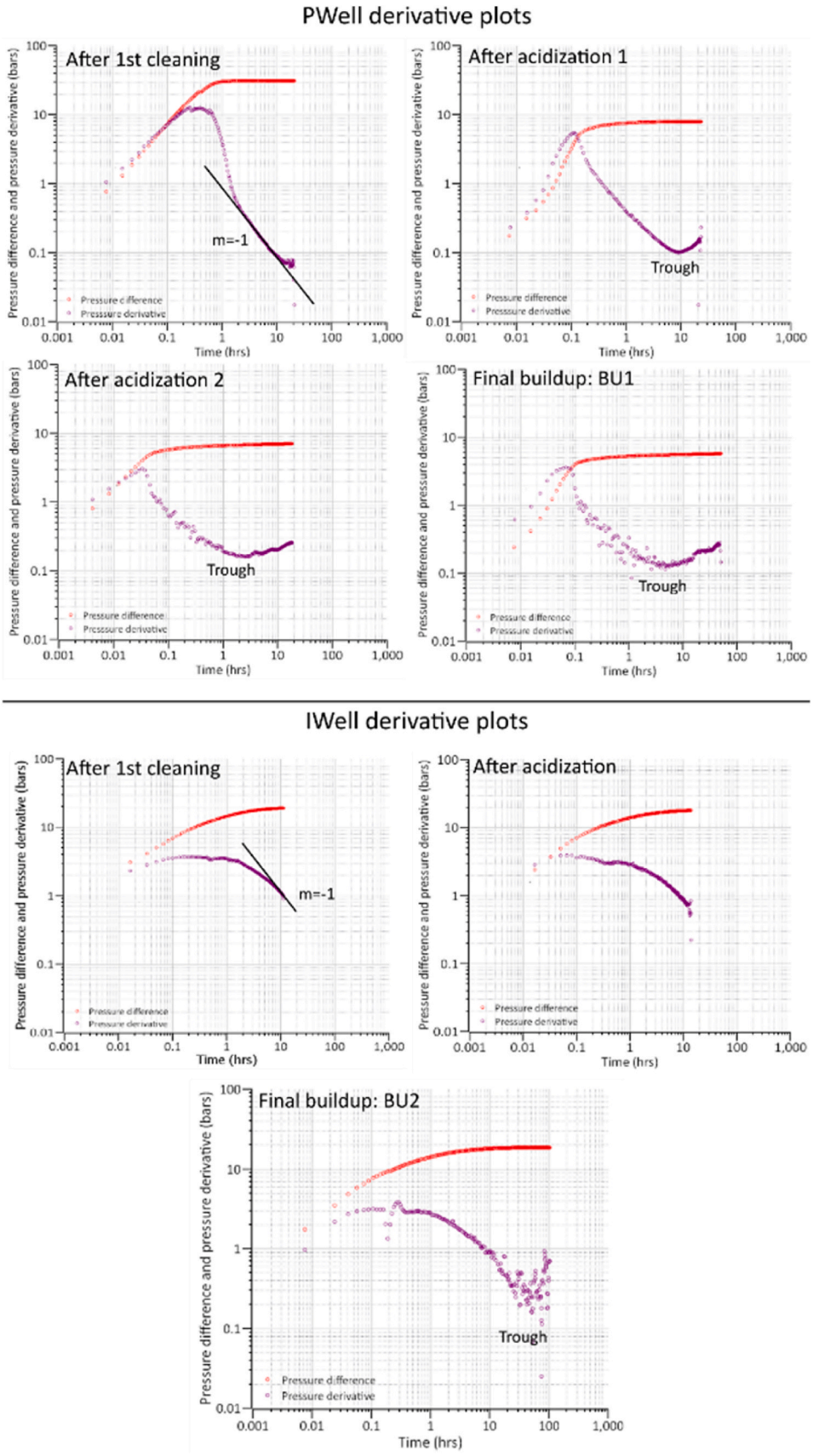

Fig. 17. Development of the double porosity behavior in the PWell (top figures) and the IWell (bottom figures) after several acidization and cleaning jobs.

the IWell are lower than the PWell, where the minimum of the trough in the IWell only appears in the last buildup test after almost 50 hrs of buildup. This is due to the weak interconnectivity between the matrix and the fractures in the IWell compared with the PWell.

Visualizing the change in the PD behavior strengthen the reliability of our interpretation that the reservoir is naturally fractured. The difference in the shape between the PD plots in the IWell and the PWell is due to their relative location within the reservoir permeability structure (Fig. 5 and section 2.3). Finally, we detect no technical issues, as each PD plot is unique, where late time behavior is characteristic for each test.

5.2. Dynamic behavior of fracture corridors

Fracture corridors consist of sub-parallel/sub-vertical densely packed fractures of variable dimensions. Their fracture density can reach three to ten fractures per meter or more. They are usually associated with fault zones or formed in weak lithological contacts, where stress field and rock strength are the main variables controlling their formation (Cooke and Underwood, 2001). Corridors have a considerable impact on the reservoir hydraulics because their permeability can reach tens of Darcy, whereas the matrix possesses permeability in the range of miliDarcy. Distinguishing fracture corridors requires the integration of multi-scale geophysical data sets (seismic and sub-seismic) in combination with dynamic hydraulic testing data (Nosjean et al., 2020).

Guo (2020) utilized the commercial software CMG® to illustrate the evolution of the characteristic fluid flow regimes of a well close to a fracture corridor through utilizing a synthetic model, without the influence of wellbore storage and skin effects (Fig. 18a and b). First, a radial flow regime may occur in the matrix around the well until the transient pressure wave reaches the corridor. The high permeability of the corridor induces a pressure drop. Following this, a trough-shaped PD curve and a bilinear flow occur, as the matrix (of high storativity) surrounding the depleted corridor (of low storativity) supports it with fluid. Finally, a second radial flow occurs once hydraulic equilibrium is reached for the whole system. It is also observable that the corridor induces a boundary effect at late time, where the PD exhibits a positive

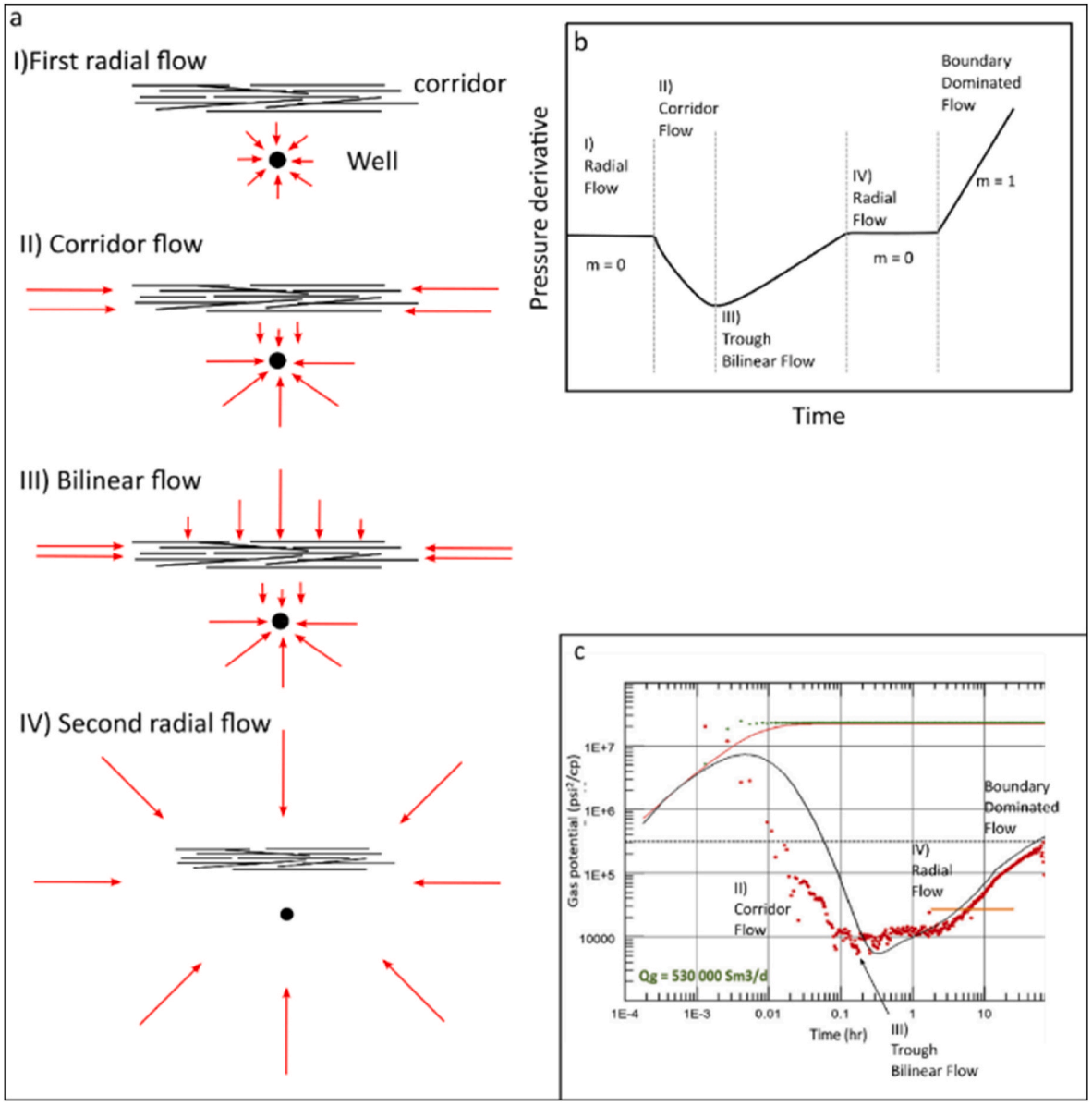

Fig. 18. Illustration of the fluid flow regimes occurring at a well in the vicinity of a fracture corridor. a) and b) are modifications from Guo (2020), which illustrate theoretically the characteristic flow regimes occurring in a reservoir accommodating a fracture corridor. c) A real-world field example of a well located in a fracture corridor modified after Nosjean et al. (2020). Notice the similarity in the PD plots between b), c) and in Fig. 9 (BU1).

straight line of m = 1.

Fig. 18c displays a field example of a PD plot derived from a Drill Stem Test of a well in a fracture corridor, including the wellbore storage effect at early time (Nosjean et al., 2020). By comparing Fig. 18b and c, we can observe a similarity in the pressure response between both studies. As seen in Fig. 9, the PD plot of BU1 has similar characteristic shape to the flowing regimes of a well close or in a fracture corridor. The first radial flow in Fig. 18b is masked in BU1 by the effect of the wellbore storage and the skin effects, similar to Fig. 18c. The trough shaped curve of BU1 is observable in both Fig. 18c and b. The second radial flow which represents the flow from the whole system is also found in BU1. Late time response of BU1 is characterized by a line of m = 1, similar to the same boundary effects observed in Fig. 18b and c. Hence, the close resemblance of the PD plots between the figures corroborates the interpretation of the fracture corridor, which is also in agreement with the geophysical and geological observations of Fadel et al. (2022).

5.3. Faults dynamic behavior of different throw magnitudes

Faults and their associated damage zones in the Malm reservoir at the GMA have been utilized as prime drilling targets for geothermal exploitation (Budach et al., 2017; Moeck, 2014; Moeck et al., 2015). They theoretically contain natural fracture networks of high permeability, providing high production/injection flow rates. However, those faults experienced complex kinematic history, where their hydraulic behavior are hard to predict (Moeck et al., 2015). Theoretically, faults tend to increase the permeability of tight rocks and impair the permeability of porous rocks (Fossen, 2010). In sedimentary reservoirs, the location of lithology juxtaposition and the variability in the fracture density between the hanging and the foot wall control the fault's permeability (Caine et al., 1996; Fossen, 2010). The variability in the faults throw magnitudes impact the fluid flow, where large throwing faults juxtapose horizons of contrasting permeability forming a juxtaposition seal, which retard mass flow perpendicular to the fault plane (Fisher and Knipe, 2001). OGIA (2020) indicated that faults, which juxtapose permeable horizons exhibit high perpendicular permeability tensor. In this context, we try to give a first insight on the possible relationship between the faults' throw magnitudes in the Malm reservoir with their hydraulic behavior observed from published well test data.

The geothermal doublet in our study is located nearby the Unterhaching (UHG) geothermal site (Lüschen et al., 2014; Wolfgramm et al., 2007). Each of the IWell (in our study) and the UHG Gt2 well penetrates faults of different throw. The IWell is penetrating the Northern Fault of 70 m throw, while the UHG Gt2 is intersecting the UHG main fault of 240 m throw (Fig. 19) (Budach et al., 2017; Lüschen et al., 2014; Ortiz Rojas et al., 2018). Hence, comparing the PD plots of BU2 (IWell) and the corresponding build-up phase of UHG Gt2 can give insight into the hydraulic behavior of faults being sealing, conductive or transparent according to their throw.

There is a difference in the shape of the PD plots between BU2 and the corresponding build-up phase in UHG Gt2 derived by Ortiz Rojas et al., 2018) (Fig. 19). The PD curve related to the UHG Gt2 middle response is dominated by a bilinear flow, recognized by a straight line of m = 0.5. The late response is dominated by a straight line of m = −1, reflecting a constant pressure boundary or an infinite conductive fault. Hence, the 240-m-throw UHG main fault is acting as a conductive fault, where the permeability component parallel to its plane is higher than the one perpendicular to it. On the other hand, the PD curve associated

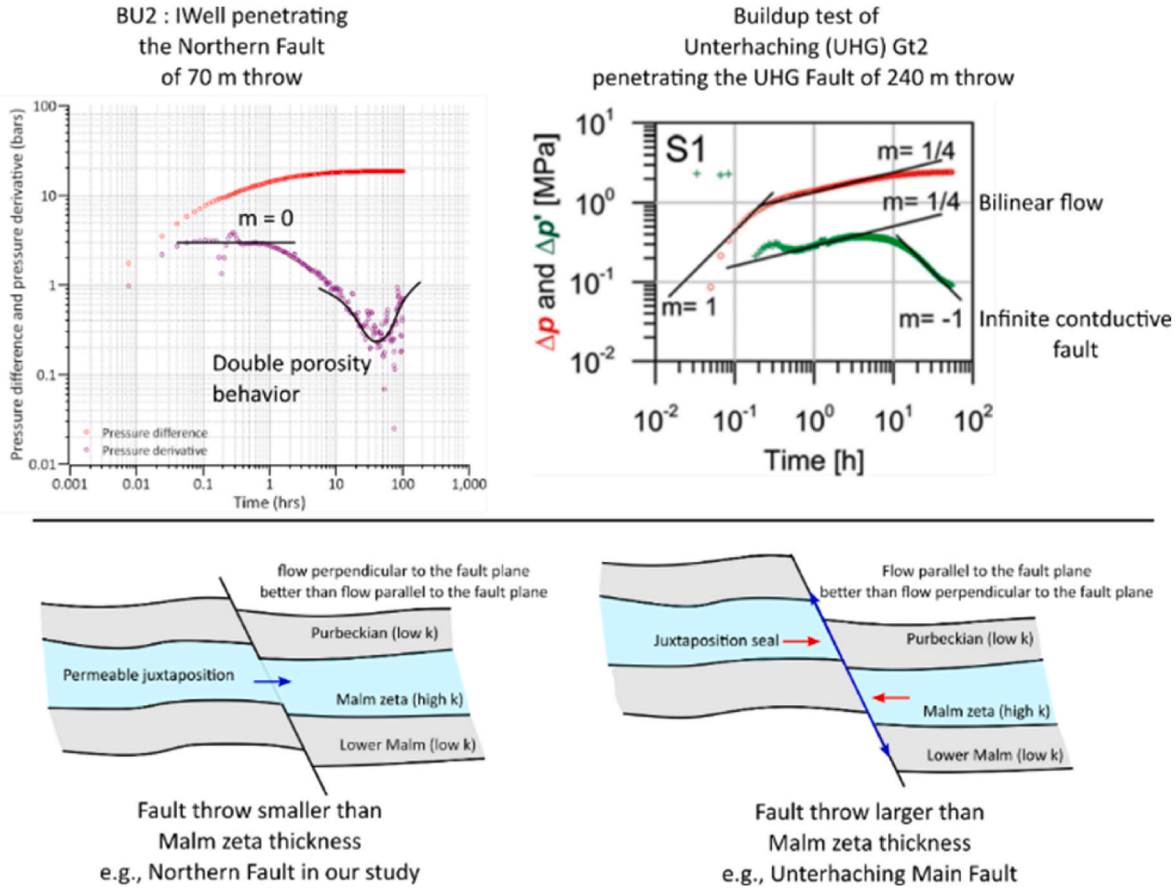

Fig. 19. Comparison between the PD plots of BU2 (upper panel left side) and the Unterhaching Gt2 (upper panel right side) modified after Ortiz Rojas et al. (2018). Both wells penetrate faults of different throw magnitudes. Note the difference in the shape of the PD curves between both plots indicating different hydraulic behavior. Bottom panel is a schematic illustrating the possible lithological juxtaposition control on the hydraulic behavior of both faults based on the throw.

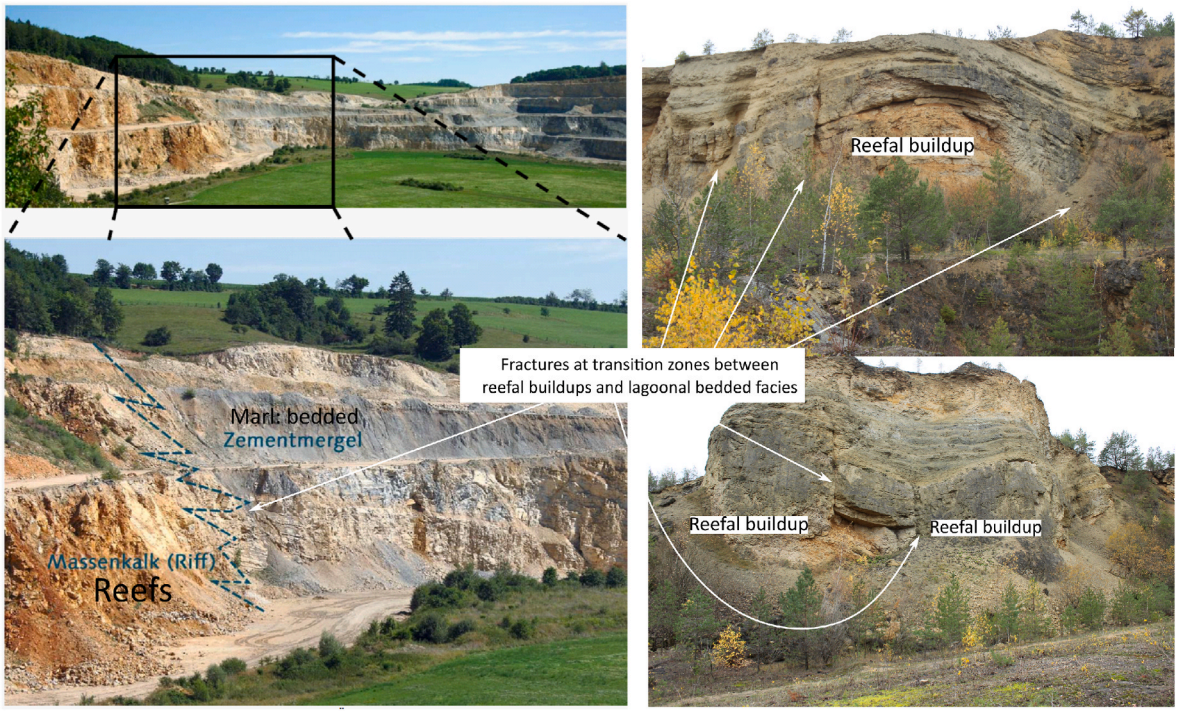

Fig. 20. Outcrops from the Malm reservoir. Left panel is modified after Homuth (2014), displaying a transitional zone dominated by high density of vertical/sub-vertical fractures. Right panel are outcrop pictures captured by Bauer et al. (2021) and Wadas and von Hartmann (2022), displaying in detail reefal buildup structures. Notice the location of vertical fractures between the reefal buildups and the adjacent bedded facies.

with BU2 shows a radial flow at the beginning, indicating that the Northern Fault is hydraulically transparent. However, the hydraulic connectivity between the Northern Fault and the fracture corridor causes a trough-shaped curve. The Northern Fault's small throw juxtapose the Upper section of the Malm reservoir (Malm Zeta), which accommodates high permeability. In contrast, the throw of the UHG main fault is larger than the Malm Zeta thickness, postulating a juxtaposition seal.

We infer that faults of large throw in the Malm reservoir could act as a conduit and seal the fluid flow perpendicular to their planes. Faults of small throw such as the Northern Fault allow the juxtaposition of Malm Zeta, where fluid flow may occur perpendicular to their plane, possibly making them transparent in the well testing data, assuming that the permeability of Malm Zeta is considerable.

5.4. Hydraulic characteristics of the Malm reservoir

Karstification is one of the main permeability attributes controlling the hydraulics of the Malm reservoir (Zosseder et al., 2022). In the northern part of the NAFB, where the Malm reservoir outcrops, the shallow well Altdorf displays a dominant radial flow due to karstification (Birner, 2013). In this region, the application of the EPM approach is feasible, as long there is a match between the reservoir static and dynamic nature. Towards the south (including the GMA), the influence of karstification decreases (Birner, 2013; Dussel et al., 2016), where inflow zones of deep geothermal wells in the GMA are rather associated with fracturing and karstified fractures (Bauer et al., 2021; Birner, 2013; Homuth et al., 2015; Savvatis, 2012; Wolfgramm et al., 2007). As the extent of karstification declines from north to south, other permeability attributes might have a more pronounced impact on the fluid flow dynamics. Hence, it is possible to observe different flowing regimes in the geothermal wells in that area.

Wadas and von Hartmann (2022) applied seismic inversion utilizing an acoustic impedance model of a 3D seismic data and porosity logs to derive a porosity model for the Malm reservoir at the Schäftlarnstraße geothermal site. The authors identified complex reef structures based on the seismic morphology and the resulting porosity model. The porosity model indicated that the reef cores have porosities <3%, while the reef capes and the reef slopes have porosities up to 14%. We refer to the reef capes and slopes in our study as transitional zones. Homuth (2014) and Homuth et al. (2015) observed from outcrop studies that transitional zones between reefal buildups and lagoonal facies contain high density of vertical/sub-vertical factures due to differential compaction and changes in rock structure/strength (Fig. 20). Hence, we propose that hight density fractures are likely the cause for the observed increase in the porosity at the reef caps and the reef slopes observed by Wadas and von Hartmann (2022). Since those fractures follow the strike of transitional zones, they can form fracture corridors and significantly influence the reservoir hydraulics. Especially if transitional zones are critically oriented like in our study.

Secondary porosity in the Malm reservoir is generated by various factors such as fault damage zones, fracturing due to burial or tectonic activities, lithofacies changes laterally and vertically, dolomitization, and karstification (Dussel et al., 2016; Homuth, 2014; Moeck et al., 2020; Wadas and von Hartmann, 2022). The hydraulic influence of those features can vary significantly depending on the location within the Malm reservoir (Birner, 2013). Therefore, we urge reservoir engineers to prioritize the primary factor that controls permeability within the scale of their study, particularly when assessing sensitive scenarios such as thermal breakthrough. For instance, if bedded lagoons dominate the geological setting and are associated with composite reservoir behavior as evidenced by PTA, then a layered reservoir model is viable. Conversely, if fractures are observed in the inflow zones and are correlated with seismic-scale structures, the implementation of fractured reservoir models becomes essential.

5.5. Malm reservoir model type

Composite-layered reservoirs exhibit similar behaviours to double porosity reservoirs in analytical models due to the non-uniqueness

nature of the problem setting. However, the problem of non-uniqueness can be constrained by observations from geophysical borehole data and geological knowledge (e.g., Bourdet, 2002). In our case, we chose a double porosity reservoir system based on clear observations of the dominance of fractures. This conclusion is also substantiated by recent findings of Wadas and von Hartmann (2022), indicating that the secondary porosity of the Malm reservoir lead to the formation of a dual porosity reservoir type. Moreover, Bauer et al. (2021) observed intense fracturing and karstified fractures within the main inflow zones of the Schäftlarnstraße (Munich city) geothermal wells, similar to the IWell and the PWell.

In contrast to classical sedimentary reservoirs where layering can be easily identified from logging and seismic data, the seismic traces within the Malm reservoir are very chaotic, where lithology and porosity logs correlation is difficult, and tracing seismic reflectors is challenging (Fadel et al., 2021; Lüschen et al., 2014; Thomas et al., 2010; Wadas and von Hartmann, 2022). Consequently, the permeability of the Malm reservoir in the GMA is dominated by secondary processes rather than the matrix system (Balcewicz et al., 2021; Bauer et al., 2021; Birner et al., 2012; Cacace et al., 2013; Ehrenberg and Nadeau, 2005; Homuth et al., 2015; Moeck et al., 2020). Hence, we suggest that the Malm carbonate reservoir in this region should be modelled as a non-layered reservoir type.

Our decision not to consider the reservoir as a layered model is also based on the results obtained from geophysical data interpretations associated with temperature/flow meter logs. The integration of these data reveals that the primary inflow zones are located at different formations and exhibit distinct characteristics:

- Zone A is dominated by the damage zone of the Northern Fault and is located at Top Malm Zeta
- Zone C is dominated by fractures striking NW and is located at the Top Purbeckian
- Zone D is dominated by NW-striking fractures but it is located below Top Malm Zeta

The conducted temperature logs after the ETB indicate that the inflow zones are hydraulically interconnected. If the reservoir is layered, one would expect to observe high permeability zones in the Purbeckian at the IWell or in Top Malm Zeta at the PWell. We suggest that layering in the Malm reservoir in our study area does not fit its static characteristics, as vertical fractures can potentially interconnect several horizons and distort the layering of the reservoir system. Moreover, the lateral change in the carbonate facies between reefal buildups and lagoons is another obstacle in defining consistent horizontal layering of averaged hydraulic properties (Meyer and Schmidt-Kaler, 1990).

5.6. Modeling approaches

Based on our results, cautiousness must be exercised when using regional scale dynamic reservoir models to investigate and predict the thermal breakthrough time between geothermal wells. We recommend conducting independent studies to integrate the static reservoir characteristics with the hydraulic behavior observed for any wells under investigation, as regional-scale models can hardly include detailed heterogeneities. Local-scale detailed reservoir static and dynamic models can provide accurate evaluation of the propagation of the cold waterfront from the injector to the producer. Moreover, we do not recommend the adoption of a single modeling methodology for the entire Malm region. Rather, we suggest that a local scale fit-for-purpose model of specific objectives can provide more confident and reliable predictions (Ringrose and Bentley, 2015).

An example of a local scale model was presented by Konrad et al. (2019). The conceptual model suggested by the authors included only two domains: a matrix and a fault damage zone. The matrix domain averaged all the hydraulic influence of the heterogeneities on a scale lower than the reservoir scale (small-scale facies changes or individual fractures) and is described as a continuum domain with average hydraulic properties. As mentioned, the sub-seismic scale heterogeneities can have a major influence on the reservoir hydraulics. Hence, we do not recommend homogenizing those features in local-scale models. Instead, we recommend prioritizing the main attribute which control the reservoir hydraulics. For example, if a fault zone is the only controller on the reservoir permeability, the model of Konrad et al. (2019) becomes viable. However, if fracture corridors, lithofacies change, scattered karstification are found to be controlling the reservoir's permeability, then it is not recommended to homogenize the influence of those features within the matrix.

Currently, we are investigating a robust approach to build a representative static reservoir model to the observed fractures in the reservoir for history matching the ETB. To achieve this, we have partitioned the reservoir section based on thickness intervals exhibiting significant hydraulic activity, namely the 200 m interval between Top Purbeckian to the upper section of Malm Zeta (Fig. 4). This is supported by previous studies such as Bohnsack et al. (2020), Homuth et al. (2015), and Wadas and von Hartmann (2022), where the authors indicated that the upper section of the Malm reservoir contains the highest permeability and being most influenced by secondary processes. To represent the fractures identified from image logs, we start with a 2D model, where the fractures is presented as vertical discreet elements. We determine the lateral extent of the Northern Fault damage zone and the fracture corridor by integrating observations from 3D seismic data and borehole logging data (section 2.3). Subsequently, we will generate a DFN model based on the statistics of the corresponding fracture sets for each of the following:

1. The fracture set associated with the fracture corridor (striking NW)
2. The fracture set associated with the Northern Fault damage zone (striking NE)
3. Two additional background fracture sets (striking N-S and W-E)

6. Conclusions

The heterogeneous permeability of the Malm reservoir results from the interaction of various paleodepositional environments, diagenetic processes, and tectonic events. It consists of seismic-scale (e.g. faults, reefal buildups, and sinkholes) and sub-seismic scale features (e.g. dolomitization, dedolomitization, karstification, fracturing, and facies). In the northern part of the North Alpine Foreland Basin (NAFB) north of the city of Munich, karstification dominates and radial flow regime was identified from well testing data as the primary flow regime. Hence, utilizing the equivalent porous media (EPM) approach in the Northern part of the Basin can be viable. However, we do not recommend homogenizing sub-seismic scale features in local scale dynamic reservoir models within the southern part of the NAFB (Greater Munich Area and south of it), with the purpose of forecasting the short- and long-term thermal-hydraulic performance. The influential hydraulic degree of sub-seismic scale features can vary significantly at the local scale from one location to another. Capturing the hydraulic influence of those features is extremely important to achieve reliable dynamic reservoir models. Hence, homogenizing specific permeability attributes or discretely representing them requires establishing a profound, sophisticated understanding of the integration of multi-scale geophysical, geological, and the well testing data interpretations at a specific reservoir scale and location.

Our study applies pressure transient analysis (PTA) on three buildup testing data (production well BU1, injection well BU2, and an interference test BU3) corresponding to a geothermal doublet, which experienced an early thermal breakthrough (ETB). The pressure derivative (PD) of BU1 and BU2 exhibits a trough-shaped curve indicating the existence of two different storativity domains in the reservoir. The interpretations from the geophysical data (at seismic and sub-seismic

scale) indicates that fractures coincide with the inflow zones along the two wells. Hence, we interpret the reservoir to be of double porosity nature, where the matrix is the high storativity/low permeability domain, and the localized fractures are the low storativity/high permeability domain. The fractures domain corresponds to an NNW – oriented fracture corridor formed in a transitional zone between a reefal buildup and lagoonal interbedded deposits. The corridor is coupled with the Northern Fault damage zone, which ultimately causes an excellent hydraulic communication between the wells possibly causing the ETB. The excellent hydraulic communication is noticeable from the interference test (BU3), where the middle time response accommodates a straight line of slope = 0.5, indicating a linear flow induced by the fracture network between the two wells.

To validate the interpretations from the PTA, we utilize analytical models for our selected interpretation models for each of the time responses. We could achieve a good match between the analytical models and the observations. To represent the hydraulic influence of the coupling between the fracture corridor and the fault damage zone, we implement a simplified fit-for-purpose 2D discrete fracture network in a numerical model derived from the combined geophysical and geological data analysis. We utilize the same hydraulic reservoir parameters magnitudes derived from the analytical calculations, which achieved a match with the observations. By systematically varying the matrix permeability and the fractures aperture magnitudes within a reasonable parameter range, we could reach a match between the pressure response of the numerical model and the analytical calculations. The match corroborates our interpretations from the PTA and the geophysical data that the observed fracture corridor dominate the reservoir hydraulics. In future studies, we will couple the temperature variable to history match the early thermal breakthrough and attain a thermally validated model.

This study shows the importance of integrating multi-disciplinary and multi-scale data sets to understand reservoir dynamics. The application of the EPM approach modeling the thermal-hydraulic behavior of the Malm reservoir without strong hydraulic and geophysical/geological evidence can generate misleading results. EPM layered local scale models can achieve hydraulic calibration due to the non-uniqueness nature of the problem setting. However, they may fail in predicting a reliable spatiotemporal propagation of cold waterfront if the reservoir is highly heterogeneous and accommodate anisotropic permeability. The suggestion that deep geothermal wells in the Malm reservoir only exhibit radial flow must be reconsidered and a re-evaluation of the well testing data is recommended. Our study shows that radial flow does not dominate the flow regime in the three investigated buildup tests, supported by geological and geophysical interpretations. Hence, the decision-making process of selecting reservoir model types should be assisted by the combined interpretation of multi-scale dynamic and static data. This will improve the predictive power of local-scale dynamic reservoir models and increase their reliability in evaluating the performance of deep heterogeneous geothermal reservoirs.

Author contribution

Mohamed Fadel: Conceptualization, Visualization, Investigation, Review, Editing, Writing, Writing – original draft, Revision. Ernesto Meneses Rioseco: Discussion, Review, Editing, Revision. Pierre-Olivier Bruna: Discussion, Review, Editing. Inga Moeck: Discussion, Study initiation.

Declaration of competing interest

The authors declare that they have no known competing financial interests or personal relationships that could have appeared to influence the work reported in this paper

Data availability

The data that has been used is confidential.

Acknowledgements

This study belongs to the project ''REgine- Holistically optimized and sustainable reservoir development for deep geothermal facilities in the Bavarian Molasse Basin by geophysical-geologically based reservoir engineering'' and is financed by the German Federal Ministry for Economic Affairs and Climate Action (Grant number 0324332B). The funding body did not influence the content of this study.

The authors thank Stadtwerke München Services GmbH for providing the seismic and the geophysical borehole data and publishing permission. The authors also appreciate the revisions of John Reinecker and David Colin Tanner on the content of the paper, and the support provided by Denis Voskov. We appreciate the input of three anonymous reviewers, whose comments improved the final state of the paper.

Finally, we thank Emerson's Exploration & Production Software business for providing the academic license of GoCAD-Paradigm and Interpret, which has been used in seismic interpretation and Pressure Transient Analysis. We have utilized the open source Inkscape vector graphics editor and SciDAVis for editing and creating the figures and the graphs of this paper. Finally, we have utilized the open source version of zotero for citation and referencing.

Appendix A. Supplementary data

Supplementary data to this article can be found online at https://doi.org/10.1016/j.geoen.2023.212072.

Appendix

The governing equation describing the 2-D hydraulic behavior of a single-phase compressible fluid in a porous medium under confined and saturated conditions is given by:

$$s_m \frac{\partial P}{\partial t} = \frac{k_m}{\eta_f}\left(\frac{\partial^2 P}{\partial x^2} + \frac{\partial^2 P}{\partial y^2}\right)$$

where s_m (Pa^{-1}) is the specific storage capacity of matrix, k_m (m^2) is the matrix permeability, η_f (Pa s) the dynamic fluid viscosity, and P is the fluid pressure. The governing equation describing the 2-D hydraulics of a fracture is given by:

$$s_f b_f \frac{\partial P}{\partial t} = \frac{T_f}{\eta_f}\ \frac{\partial^2 P}{\partial x^2} + \frac{q_{f(x,t)}}{h}$$

where s_f (Pa^{-1}) is the specific storage capacity of fracture, b_f (m) is its aperture, T_f (m^3) is the fracture conductivity, which is controlled by the cubic law, h (m) is the fracture height, and $q_{f(x,t)}$ describes the fluid flow between the matrix and the fracture. The pressure diffusivity equations for the matrix and the fractures are coupled by $q_{f(x,t)}$, which is defined as:

$$\frac{q_{f(x,t)}}{h} = 2\frac{k_m}{\eta_f}\frac{dp}{dy}\Big|$$

where the factor 2 represents the two faces of the fracture relatively to the matrix.

References

Agemar, T., Weber, J., Schulz, R., 2014. Deep geothermal energy production in Germany. Energies 7, 4397–4416. https://doi.org/10.3390/en7074397.

Bachmann, G.H., Müller, M., Weggen, K., 1987. Evolution of the Molasse Basin (Germany, Switzerland). Tectonophys., Compressional Intra-Plate Deformations Alpine Foreland 137, 77–92. https://doi.org/10.1016/0040-1951(87)90315-5.

Bagrintseva, K.I., 2015. Carbonate Reservoir Rocks. Wiley, Hoboken, NJ.

Balcewicz, M., Ahrens, B., Lippert, K., Saenger, E.H., 2021. Characterization of discontinuities in potential reservoir rocks for geothermal applications in the Rhine-Ruhr metropolitan area (Germany). Solid Earth 12, 35–58. https://doi.org/10.5194/se-12-35-2021.

Barenblatt, G.I., Zheltov, Iu.P., Kochina, I.N., 1960. Basic concepts in the theory of seepage of homogeneous liquids in fissured rocks [strata]. J. Appl. Math. Mech. 24, 1286–1303. https://doi.org/10.1016/0021-8928(60)90107-6.

Bauer, J., Pfrang, D., Krumbholz, M., 2021. Characterisation of a Highly Heterogeneous Geothermal Reservoir Based on Geophysical Well Logs (Other). pico. https://doi.org/10.5194/egusphere-egu21-2205.

Birner, J., 2013. Hydrogeologisches Modell des Malmaquifers im Süddeutschen Molassebecken. https://doi.org/10.17169/refubium-5694.

Birner, J., Fritzer, T., Jodocy, M., Savvatis, A., Schneider, M., Stober, I., 2012. Hydraulische Eigenschaften des Malmaquifers im Süddeutschen Molassebecken und ihre Bedeutung für die geothermische Erschließung. Z. Geol. Wiss. 40, 33–56.

Blank, L., Meneses Rioseco, E., Caiazzo, A., Wilbrandt, U., 2021. Modeling, simulation, and optimization of geothermal energy production from hot sedimentary aquifers. Comput. Geosci. 25, 67–104. https://doi.org/10.1007/s10596-020-09989-8.

Bohnsack, D., Potten, M., Pfrang, D., Wolpert, P., Zosseder, K., 2020. Porosity–permeability relationship derived from Upper Jurassic carbonate rock cores to assess the regional hydraulic matrix properties of the Malm reservoir in the South German Molasse Basin. Geoth. Energy 8, 12. https://doi.org/10.1186/s40517-020-00166-9.

Bourdet, D., 2002. Well test analysis: the use of advanced interpretation models, first ed. In: Handbook of Petroleum Exploration and Production. Elsevier, Amsterdam Boston.

Bourdet, D., Gringarten, A.C., 1980. Determination of fissure volume and block size in fractured reservoirs by type-curve analysis. In: Presented at the SPE Annual Technical Conference and Exhibition. OnePetro. https://doi.org/10.2118/9293-MS.

Bourdet, D., Whittle, T.M., Douglas, A.A., Pirard, Y.M., 1983. A New Set of Type Curves Simplifies Well Test Analysis. Gulf Publishing Co., Houston, pp. 77–87.

Bradley, D.C., Kidd, W.S.F., 1991. Flexural extension of the upper continental crust in collisional foredeeps. GSA Bull. 103, 1416–1438. https://doi.org/10.1130/0016-7606(1991)103<1416:FEOTUC>2.3.CO;2.

BRG, 2018a. Flowmeter messung für IWell (Presentation).

BRG, 2018b. Druck-und Temperaturprofilmessung für PWell (Presentation).

Budach, I., Moeck, I., Lüschen, E., Wolfgramm, M., 2017. Temporal evolution of fault systems in the upper Jurassic of the Central German Molasse Basin: case study unterhaching. Int. J. Earth Sci. https://doi.org/10.1007/s00531-017-1518-1.

Bundschuh, J., Arriaga, M.C.S., 2011. Introduction to the Numerical Modeling of Groundwater and Geothermal Systems: Fundamentals of Mass, Energy and Solute Transport in Poroelastic Rocks. CRC Press, London. https://doi.org/10.1201/b10499.

Cacace, M., Blöcher, G., Watanabe, N., Moeck, I., Börsing, N., Scheck-Wenderoth, M., Kolditz, O., Huenges, E., 2013. Modelling of fractured carbonate reservoirs: outline of a novel technique via a case study from the Molasse Basin, southern Bavaria, Germany. Environ. Earth Sci. 70, 3585–3602. https://doi.org/10.1007/s12665-013-2402-3.

Caine, J.S., Evans, J.P., Forster, C.B., 1996. Fault zone architecture and permeability structure. Geology 24, 1025–1028. https://doi.org/10.1130/0091-7613(1996)024<1025:FZAAPS>2.3.CO, 2.

Chopra, S., Marfurt, K.J., 2007. Seismic Attributes for Prospect Identification and Reservoir Characterization. Society of Exploration Geophysicists and European Association of Geoscientists and Engineers. https://doi.org/10.1190/1.9781560801900.

Clark, D.G., Van Golf-Racht, T.D., 1985. Pressure-derivative approach to transient test analysis: a high-permeability North Sea Reservoir Example (includes associated papers 15270 and 15320). J. Petrol. Technol. 37, 2023–2039. https://doi.org/10.2118/12959-PA.

Cooke, M.L., Underwood, C.A., 2001. Fracture termination and step-over at bedding interfaces due to frictional slip and interface opening. J. Struct. Geol. 23, 223–238. https://doi.org/10.1016/S0191-8141(00)00092-4.

Da Prat, G., 1990. Well Test Analysis for Fractured Reservoir Evaluation, Developments in Petroleum Science. Elsevier, Amsterdam New York.

Deruyck, B.G., Bourdet, D.P., DaPrat, G., Ramey, H.J., 1982. Interpretation of interference tests in reservoirs with double porosity BehaviorTheory and field examples. In: Presented at the SPE Annual Technical Conference and Exhibition. OnePetro. https://doi.org/10.2118/11025-MS.

Djebbar, T., Anil, K., 1980. Detection and location of two parallel sealing faults around a well. J. Petrol. Technol. 32, 1701–1708. https://doi.org/10.2118/6056-PA.

Dornstadter, J., Kappelmeyer, O., Welter, M., 1999. The geothermal potential in the Upper Rhine Graben valley. In: European Geothermal Conference Basel. Presented at the European Geothermal Conference, Basel, p. 9.

Dussel, M., Lüschen, E., Thomas, R., Agemar, T., Fritzer, T., Sieblitz, S., Huber, B., Birner, J., Schulz, R., 2016. Forecast for thermal water use from upper Jurassic carbonates in the Munich region (south German Molasse Basin). Geothermics 60, 13–30. https://doi.org/10.1016/j.geothermics.2015.10.010.

Egya, D.O., Corbett, P.W.M., Geiger, S., Norgard, J.-P., Hegndal-Andersen, S., 2022. Calibration of naturally fractured reservoir models using integrated well-test analysis – an illustration with field data from the Barents Sea. Petrol. Geosci. 28, petgeo2020–p2042. https://doi.org/10.1144/petgeo2020-042.

Ehrenberg, S.N., Nadeau, P.H., 2005. Sandstone vs. carbonate petroleum reservoirs: a global perspective on porosity-depth and porosity-permeability relationships. Bulletin 89, 435–445. https://doi.org/10.1306/11230404071.

Fadel, M., Reinecker, J., Bruss, D., Moeck, I., 2022. Causes of a premature thermal breakthrough of a hydrothermal project in Germany. Geothermics 105, 102523. https://doi.org/10.1016/j.geothermics.2022.102523.

Fadel, M., Reinecker, J., Kreuter, H., 2021. Application of seismic and geomechanical approaches in defining geothermal targets in the German Molasse Basin. In: Presented at the World Geothermal Congress 2020+1, Reykjavik.

Fischedick, M., 2022. Energieversorgungsrisiken, Energiepreiskrise und Klimaschutz erfordern gemeinsame Antworten. Wirtschaftsdienst 102, 262–269. https://doi.org/10.1007/s10273-022-3163-y.

Fisher, Q.J., Knipe, R.J., 2001. The permeability of faults within siliciclastic petroleum reservoirs of the North Sea and Norwegian Continental Shelf. Mar. Petrol. Geol. 18, 1063–1081. https://doi.org/10.1016/S0264-8172(01)00042-3.

Fossen, H., 2010. Structural Geology. Cambridge University Press, Cambridge. https://doi.org/10.1017/CBO9780511777806.

Franz, M., Nowak, K., Niegel, S., Seidel, E., Wolf, M., Wolfgramm, M., 2018. Deep geothermal resources of the North German Basin: the hydrothermal reservoirs of the Stuttgart Formation (Schilfsandstein, Upper Triassic). Z. Dtsch. Ges. Geowiss. 353–387. https://doi.org/10.1127/zdgg/2018/0164.

Freudenberger, W., Schwerd, K., 1996. Erläuterungen zur Geologischen Karte von Bayern 1:500000. Bayerisches Geologisches Landesamt, Munich.

Galvao, M.S.C., Carvalho, M.S., Barreto, A.B., 2020. Thermal impacts on pressure transient tests using a coupled wellbore/reservoir analytical model. J. Petrol. Sci. Eng. 191, 106992 https://doi.org/10.1016/j.petrol.2020.106992.

GeotIS, 2022. Geothermal Information System for Germany. https://doi.org/10.17616/R3M89J.

GTN, 2010. Verlauf, Messdaten und Auswertung der Stimulations- und Testarbeiten an der Bohrung IWell (Internal report).

GTN, 2009. Durchführung und hydraulische Auswertung der Stimulations- und Testarbeiten an der Bohrung (PWell) (Internal report).

Guo, Y., 2020. Well Testing of Fracture Corridors in Naturally - Fractured Reservoirs (NFR) (Master's Thesis). The Graduate Faculty of the Louisiana State University and Agricultural and Mechanical College, Louisiana.

Homuth, S., 2014. Aufschlussanalogstudie zur Charakterisierung oberjurassischer geothermischer Karbonatreservoire im Molassebecken (PhD dissertation). Technischen Universität Darmstadt, Darmstadt.

Homuth, S., Götz, A.E., Sass, I., 2015. Reservoir characterization of the Upper Jurassic geothermal target formations (Molasse Basin, Germany): role of thermofacies as exploration tool. Geotherm. Energy Scie. 3, 41–49. https://doi.org/10.5194/gtes-3-41-2015.

Houzé, O., Viturat, D., Fjaere, O.S., 2021. The theory and practice of pressure transient analysis. In: Rate Transient Analysis, Formation Testing, Production Logging and the Use of Permanent Downhole Gauges. KAPPA Engineering.

Kikani, J., Walkup Jr., G.W., 1991. Analysis of pressure-transient tests for composite naturally fractured reservoirs. SPE Form. Eval. 6, 176–182. https://doi.org/10.2118/19786-PA.

Koch, R., 2000. Die neue Interpretation der Massenkalke des Süddeutschen Malm und ihr Einfluß auf die Qualität von Kalksteinen für technische Anwendungen. Archeaopterix 18, 43–65.

Konrad, F., Savvatis, A., Degen, D., Wellmann, F., Einsiedl, F., Zosseder, K., 2021. Productivity enhancement of geothermal wells through fault zones: efficient numerical evaluation of a parameter space for the Upper Jurassic aquifer of the

North Alpine Foreland Basin. Geothermics 95, 102119. https://doi.org/10.1016/j.geothermics.2021.102119.
Konrad, F., Savvatis, A., Wellmann, F., Zosseder, K., 2019. Hydraulic behavior of fault zones in pump tests of geothermal wells: a parametric analysis using numerical simulations for the Upper Jurassic aquifer of the North Alpine Foreland Basin. Geoth. Energy 7, 25. https://doi.org/10.1186/s40517-019-0137-4.
Kuchuk, F., Biryukov, D., Fitzpatrick, T., 2015. Fractured-reservoir modeling and interpretation. SPE J. 20, 983–1004. https://doi.org/10.2118/176030-PA.
Leinfelder, R.R., 2001. In: Stanley, G.D. (Ed.), Jurassic reef ecosystems, The History and Sedimentology of Ancient Reef Systems, Topics in Geobiology. Springer US, Boston, MA, pp. 251–309. https://doi.org/10.1007/978-1-4615-1219-6_8.
Lüschen, E., Wolfgramm, M., Fritzer, T., Dussel, M., Thomas, R., Schulz, R., 2014. 3D seismic survey explores geothermal targets for reservoir characterization at Unterhaching, Munich, Germany. Geothermics 50, 167–179. https://doi.org/10.1016/j.geothermics.2013.09.007.
Mavor, M.J., Cinco-Ley, H., 1979. Transient pressure behavior of naturally fractured reservoirs. In: Presented at the SPE California Regional Meeting. OnePetro. https://doi.org/10.2118/7977-MS.
Mayolle, S., Soliva, R., Caniven, Y., Wibberley, C., Ballas, G., Milesi, G., Dominguez, S., 2019. Scaling of fault damage zones in carbonate rocks. J. Struct. Geol. 124, 35–50. https://doi.org/10.1016/j.jsg.2019.03.007.
Meneses Rioseco, E., Dussel, M., Moeck, I.S., 2022. 3D thermo-hydro-mechanical simulation of the behaviour of a naturally fractured petrothermal reservoir in deep Upper Jurassic carbonates of the Bavarian Molasse Basin – case study Geretsried. Geomech. Tunnell. 15, 48–57. https://doi.org/10.1002/geot.202100083.
Meneses Rioseco, E., Ziesch, J., Wawerzinek, B., Hartmann, H.V., Thomas, R., Buness, H., 2018. 3-D geothermal reservoir modeling of the upper Jurassic Carbonate Aquifer in the City of Munich (Germany) under the thermal-hydraulic influence of optimized geothermal multi-well patterns - project GeoParaMoL. In: Presented at the 43rd Workshop on Geothermal Reservoir Engineering, California, p. 12.
Meyer, R.K.F., Schmidt-Kaler, H., 1990. Paläogeographie und Schwammriffentwicklung des süddeutschen Malm—ein Überblick. Facies 23, 175–184. https://doi.org/10.1007/BF02536712.
Miller Frank, G., 1962. Theory of unsteady-state influx of water in linear reservoirs. J. Inst. Petrol. 48, 365–379.
Moeck, I., 2014. Catalog of geothermal play types based on geologic controls. Renew. Sustain. Energy Rev. 37, 867–882. https://doi.org/10.1016/j.rser.2014.05.032.
Moeck, I., Uhlig, S., Loske, B., Jentsch, A., Mählmann, R.F., Hild, S., 2015. Fossil multiphase normal faults - prime targets for geothermal drilling in the Bavarian Molasse Basin?. In: World Geothermal Congress 2015. Australia, p. 7.
Moeck, I.S., Dussel, M., Weber, J., Schintgen, T., Wolfgramm, M., 2020. Geothermal play typing in Germany, case study Molasse Basin: a modern concept to categorise geothermal resources related to crustal permeability. Neth. J. Geosci. 98, e14. https://doi.org/10.1017/njg.2019.12.
Mraz, E., Moeck, I., Bissmann, S., Hild, S., 2018. Multiphase fossil normal faults as geothermal exploration targets in the Western Bavarian Molasse Basin: case study Mauerstetten. zdgg 169, 389–411. https://doi.org/10.1127/zdgg/2018/0166.
Nosjean, N., Khamitov, Y., Rodriguez, S., Yahia-Cherif, R., 2020. Fracture corridor identification through 3D multifocusing to improve well deliverability, an Algerian tight reservoir case study. Solid Earth Sci. 5, 31–49. https://doi.org/10.1016/j.sesci.2019.11.009.
Nutakki, R., Mattar, L., 1982. Pressure transient analysis of wells in very long narrow reservoirs. In: Presented at the SPE Annual Technical Conference and Exhibition. OnePetro. https://doi.org/10.2118/11221-MS.
OGIA, 2020. Hydrogeological Characterisation of Faults in the Surat Basin: Assessing Fault-Induced Connectivity between the Walloon Coal Measures and Adjacent Aquifers. Department of Regional Development, Manufacturing and Water, Brisbane.
Ortiz Rojas, A.E., Dussel, M., Moeck, I., 2018. Borehole geophysical characterisation of a major fault zone in the geothermal Unterhaching Gt 2 well, South German Molasse Basin. zdgg 169, 445–463. https://doi.org/10.1127/zdgg/2017/0128.
Pawellek, T., Aigner, T., 2004. Dynamic stratigraphy as a tool in economic mineral exploration: ultra-pure limestones (Upper Jurassic, SW Germany). Mar. Petrol. Geol., Econ. Appl. Sedimentol. 21, 499–516. https://doi.org/10.1016/S0264-8172(03)00093-X.
Pei, L., Blöcher, G., Milsch, H., Zimmermann, G., Sass, I., Huenges, E., 2018. Thermo-mechanical properties of upper Jurassic (Malm) carbonate rock under drained conditions. Rock Mech. Rock Eng. 51, 23–45. https://doi.org/10.1007/s00603-017-1313-0.
Reinecker, J., Tingay, M., Müller, B., Heidbach, O., 2010. Present-day stress orientation in the Molasse Basin. Tectonophys., Front. Stress Res. 482, 129–138. https://doi.org/10.1016/j.tecto.2009.07.021.
Ringrose, P., Bentley, M., 2015. Reservoir Model Design: A Practitioner's Guide. Springer, Dordrecht Heidelberg.
Saldana, -C.M.A., Ramey, H.J., 1986. Slug test and drillstem test flow phenomena including wellbore inertial and frictional effects. In: SPE California Regional Meeting. Presented at the SPE California Regional Meeting. Society of Petroleum Engineers, Oakland, California. https://doi.org/10.2118/15118-MS.
Savvatis, A., 2012. In: Schneider, M., Thomas, L. (Eds.), Hydraulik, Wissenschaftliche Und Technische Grundlagen Zur Strukturgeologischen Und Hydrogeologischen Charakterisierung Tiefer Geothermisch Genutzter Grundwasserleiter Am Beispiel Des Süddeutschen Molassebeckens. Bundesministerium für Umwelt, Naturschutz und Reaktorsicherheit, Projektträger Jülich (PTJ-EEN), pp. 129–154.
Schiffer, H.-W., Trüby, J., 2018. A review of the German energy transition: taking stock, looking ahead, and drawing conclusions for the Middle East and North Africa. Energy Transit 2, 1–14. https://doi.org/10.1007/s41825-018-0010-2.
Schmid, D., Leinfelder, R., Schweigert, G., 2005. Stratigraphy and palaeoenvironments of the upper Jurassic of southern Germany – a review. Zitteliana Reihe B: Abhandlungen der Bayerischen Staatssammlung fur Palaontologie und Geologie 26, 31–41.
Schulz, R., Thomas, R., Dussel, M., Lüschen, E., Wenderoth, F., Fritzer, T., Birner, J., Schneider, M., Wolfgramm, M., Bartels, J., Hiber, B., Megies, T., Wassermann, J., 2012. Geothermische Charakterisierung von karstig-klüftigen Aquiferen im Großraum München (No. 0325013A). Leibniz-Institut für Angewandte Geophysik (LIAG), Hannover, Niedersachsen.
Streltsova, T.D., 1988. Well Testing in Heterogeneous Formations. Wiley, New York.
Thomas, R., Lueschen, E., Schulz, R., 2010. Seismic reflection exploration of Karst phenomena of a geothermal reservoir in southern Germany. In: Presented at the World Geothermal Congress 2010, Bali, Indonesia, p. 8.
von Hartmann, H., Buness, H., Krawczyk, C.M., Schulz, R., 2012. 3-D seismic analysis of a carbonate platform in the Molasse Basin - reef distribution and internal separation with seismic attributes. Tectonophys., Seismic Imag. Continent. Margin.: N. Res. Confluence Active Passive Seismol. 572–573, 16–25. https://doi.org/10.1016/j.tecto.2012.06.033.
Wadas, S.H., von Hartmann, H., 2022. Porosity estimation of a geothermal carbonate reservoir in the German Molasse Basin based on seismic amplitude inversion. Geoth. Energy 10, 13. https://doi.org/10.1186/s40517-022-00223-5.
Wagner, W., Kretzschmar, H.-J., 2008. International Steam Tables - Properties of Water and Steam Based on the Industrial Formulation IAPWS-IF97. Springer-Verlag, Berlin.
Warren, J.E., Root, P.J., 1963. The behavior of naturally fractured reservoirs. Soc. Petrol. Eng. J. 3, 245–255. https://doi.org/10.2118/426-PA.
Wolfgramm, M., Bartels, J., Hoffmann, F., Kittl, G., Lenz, G., Seibt, P., Schulz, R., Thomas, R., Unger, H.J., 2007. Unterhaching geothermal well doublet: structural and hydrodynamic reservoir characteristic; Bavaria (Germany). In: Presented at the European Geothermal Congress 2007, Unterhaching, Germany, p. 6.
Wong, D.W., Mothersele, C.D., Harrington, A.G., Cinco-Ley, H., 1986. Pressure transient analysis in finite linear reservoirs using derivative and conventional Techniques: field examples. In: Presented at the SPE Annual Technical Conference and Exhibition. OnePetro. https://doi.org/10.2118/15421-MS.
Zarrouk, S.J., McLean, K., 2019. Geothermal Well Test Analysis: Fundamentals, Applications and Advanced Techniques. Academic Press.
Ziegler, M.O., Heidbach, O., Reinecker, J., Przybycin, A.M., Scheck-Wenderoth, M., 2016. A multi-stage 3-D stress field modelling approach exemplified in the Bavarian Molasse Basin. Solid Earth 7, 1365–1382. https://doi.org/10.5194/se-7-1365-2016.
Zosseder, K., Pfrang, D., Schölderle, F., Bohnsack, D., Konrad, F., 2022. Characterisation of the Upper Jurassic geothermal reservoir in the South German Molasse Basin as basis for a potential assessment to foster the geothermal installation development – results from the joint research project Geothermal Alliance Bavaria. Geomech. Tunnell. 15, 17–24. https://doi.org/10.1002/geot.202100087.